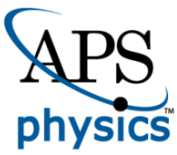

Net-baryon diffusion in fluid-dynamic simulations of relativistic heavy-ion collisions

Gabriel S. Denicol, Charles Gale, Sangyong Jeon, Akihiko Monnai, Björn Schenke, and Chun Shen

Phys. Rev. C **98**, 034916 — Published 24 September 2018

DOI: 10.1103/PhysRevC.98.034916

Net baryon diffusion in fluid dynamic simulations of relativistic heavy-ion collisions

Gabriel S. Denicol,[1] Charles Gale,[2] Sangyong Jeon,[2] Akihiko Monnai,[3,4] Björn Schenke,[5] and Chun Shen[5]

[1]*Instituto de Física, Universidade Federal Fluminense, UFF, Niterói, 24210-346, RJ, Brazil*
[2]*Department of Physics, McGill University, 3600 University Street, Montreal, QC, H3A 2T8, Canada*
[3]*Institut de Physique Théorique, CNRS, CEA/Saclay, F-91191 Gif-sur-Yvette, France*
[4]*KEK Theory Center, Institute of Particle and Nuclear Studies, High Energy Accelerator Research Organization (KEK), 1-1, Ooho, Tsukuba, Ibaraki 305-0801, Japan*
[5]*Physics Department, Brookhaven National Laboratory, Upton, NY 11973, USA*

A hybrid (hydrodynamics + hadronic transport) theoretical framework is assembled to model the bulk dynamics of relativistic heavy-ion collisions at energies accessible in the Beam Energy Scan (BES) program at the Relativistic Heavy-Ion Collider (RHIC) and the NA61/SHINE experiment at CERN. The system's energy-momentum tensor and net baryon current are evolved according to relativistic hydrodynamics with finite shear viscosity and non-zero net baryon diffusion. Our hydrodynamic description is matched to a hadronic transport model in the dilute region. With this fully integrated theoretical framework, we present a pilot study of the hadronic chemistry, particle spectra, and anisotropic flow. Phenomenological effects of a non-zero net-baryon current and its diffusion on hadronic observables are presented for the first time. The importance of the hadronic transport phase is also investigated.

PACS numbers: 12.38.Mh, 47.75.+f, 47.10.ad, 11.25.Hf

I. INTRODUCTION

The beam energy scan program (BES and BESII) at the Relativistic Heavy Ion Collider (RHIC) at Brookhaven National Laboratory [1–4] and the NA61/SHINE experiment at the CERN Super Proton Synchrotron (SPS) [5] aim to fully explore the phase diagram of strongly interacting matter. In the baryon-rich region, the transition from a hadron gas to a quark-gluon-plasma phase (QGP) is expected to be first order, whereas it is a rapid crossover at the low baryon density. Therefore, the existence of a critical point in this phase diagram is widely speculated. The existence of such a critical point has yet to be confirmed, and its location in the phase diagram determined.

Measurements sensitive to the presence of a critical point are those of fluctuations of conserved charges, most commonly those of net-baryon number. In the vicinity of a critical point, the correlation length grows, leading to increased fluctuations [6–8]. Varying the collision energy should then allow the trajectory of the system to explore the plane spanned by temperature and baryon chemical potential, and to locate the position of the critical point using the fluctuation measurements.

To accomplish this, one needs to know precisely what to expect for the relevant observables in the case that there is no critical point (and fluctuations are entirely non-critical) and how they are modified if a critical point is present. This requires complex simulations of the entire system starting from fluctuating initial states, hydrodynamic evolution at finite net-baryon density (and possible hydrodynamic fluctuations [9–11]), as well as microscopic hadronic cascades for the low temperature stage [12–17].

Such simulations can then be used to study the effects of an equation of state with a critical point [18]. They can be coupled to evolution equations for the sigma field and Polyakov loop in the so called chiral fluid dynamics [19, 20], and can provide important information required for calculations of the non-equilibrium evolution of cumulants of critical fluctuations [21].

Calculations that include the viscous relativistic hydrodynamic evolution of the QGP and hadron gas, combined with models for fluctuating initial states and hadronic afterburners, have been very successful in describing the soft observables measured in heavy ion collisions at top RHIC and Large Hadron Collider (LHC) energies. However, at these high collision energies the net-baryon density is typically assumed to be negligible, which is valid at least near mid-rapidity [16]. Furthermore, the initial state description is somewhat simplified because an instantaneous interaction of two highly contracted nuclei can be assumed. At lower energies, neither assumption holds. For reviews on relativistic hydrodynamics and hybrid models of heavy ion collisions we refer the reader to [22, 23] and [24], respectively.

To make progress towards a simulation framework valid at all collision energies, fluctuating initial conditions for lower energy collisions have been addressed recently [13, 16, 25]. In this work we focus on the effects of an improved description of baryon transport in the hydrodynamic description of heavy ion collisions, and will not consider initial state fluctuations. The simulation MUSIC[1] [26] has included the evolution of conserved baryon currents from the beginning, but baryon diffusion has so far been neglected. However, when studying observables that are sensitive to the precise baryon distributions and

[1] The numerical package can be downloaded from http://www.physics.mcgill.ca/music.

their fluctuations [27], we need to take great care in including all relevant physics in the simulation. In this work we present results of an extended version of MUSIC that includes the most basic effects of baryon diffusion.

Apart from this extension of the hydrodynamic simulation itself, we need to consider an equation of state at finite baryon density. We present a construction of such an equation of state using Lattice QCD results with Taylor expansion in baryon chemical potential coupled to a hadron resonance gas, and use it in all shown calculations. Current lattice QCD simulations have not shown evidence of a critical point and, hence, our results at this stage do not probe any effects from a critical point – hence, in this aspect, they can be considered as baseline calculations.

Besides providing a necessary tool for simulating heavy ion collisions over a wide range of energies relevant to the critical point search, the new developments presented in this work also establish a path to the extraction of the heat conductivity of the quark gluon plasma by detailed comparison with experimental measurements. We identify observables that are most sensitive to the effect of baryon diffusion and thus the heat conductivity of the QGP.

The paper is organized as follows. Sec. II gives a detailed model description of our hybrid framework. The phenomenological impact of net baryon diffusion and hadronic transport on experimental observables are studied in Sec. III. The focus of our studies are Au+Au collisions at 19.6 GeV. Sec. IV summarizes the main findings of this work. Additional detailed derivations of net baryon diffusion corrections and numerical validation of the hydrodynamic simulation are presented in the appendices.

II. THE HYBRID FRAMEWORK

A. Initialization of hydrodynamics

For very high center of mass energies, like the top RHIC energy or LHC energies, the Lorentz contraction of the incoming nuclei is so strong that it is a good approximation to consider them as sheets of negligible width in the longitudinal (beam-) direction. This means that the time of the collision is given precisely by the time the two sheets pass through each other. In contrast, the collision energies scanned in the RHIC BES program and the NA61/SHINE experiment are not high enough to neglect the finite thickness of the colliding nuclei along the longitudinal direction. The time the two nuclei spend passing through one another for a given collision energy $\sqrt{s_{\rm NN}}$ can be estimated as

$$\tau_{\rm overlap} = \frac{2R}{\gamma_L v_L} = \frac{2R}{\sqrt{\gamma_L^2 - 1}}, \tag{1}$$

where the Lorentz factor in the longitudinal direction is $\gamma_L = \frac{\sqrt{s_{\rm NN}}/2}{m_N}$ with $m_N = 0.938$ GeV, and R is the radius of the colliding nuclei. For gold nuclei $R_{\rm Au} \simeq 7.0\,$fm. At the lowest BES collision energy of $\sqrt{s_{\rm NN}} = 7.7$ GeV, this overlapping time is 3 fm, comparable to the lifetime of the QGP created in the system.

In Ref. [16] two of the authors have presented a new initial state model that treats the early stage of the evolution dynamically by starting hydrodynamic evolution before that time and taking care of additional deposited entropy and baryon densities via source terms.

Because the focus of this work is the effect of baryon diffusion, we employ a simpler initial state description, where the initial entropy and baryon densities are assumed to be smooth average quantities and the hydrodynamic simulations are started at $\tau_0 = \tau_{\rm overlap}$. The smooth initial conditions are generated by averaging over 10,000 fluctuating Monte Carlo (MC)-Glauber events in the given centrality bin, which is determined using the configurations' total entropy at mid-rapidity. When averaging the spatial structure, events within the same centrality bin are aligned using their second-order participant plane angles, $\Psi_2^{\rm PP}$, defined as

$$\varepsilon_2 e^{i2\Psi_2^{\rm PP}} = -\frac{\int d^2\mathbf{r}\, r^2 s(r,\phi) e^{i2\phi}}{\int d^2\mathbf{r}\, r^2 s(r,\phi)}. \tag{2}$$

Here $s(r,\phi)$ is the transverse plane entropy density profile at mid-rapidity.

To construct the entropy density as a function of the transverse coordinates and of the space-time rapidity, we first define the contributions from the right moving (+) and left moving (−) nuclei as

$$s_\pm(x,y) = \sum_{j=1}^{N_{\rm part}^\pm} \frac{1}{2\pi\sigma^2} \exp\left(-\frac{(\mathbf{r}-\mathbf{r}_j^\pm)^2}{2\sigma^2}\right), \tag{3}$$

where $\mathbf{r} = (x,y)$ and $\mathbf{r}_j^\pm$ are the positions of the participant nucleons in the two nuclei. The Gaussian width parameter is set to $\sigma = 0.5$ fm. Because we will use the event-averaged initial density profile as the initial condition for hydrodynamic simulations, the choice of σ will not affect our results.

The full initial 3D density profiles follow from folding $s_\pm(x,y)$ with envelope functions along the rapidity direction,

$$s(x,y,\eta;\tau_0) = \frac{s_0}{\tau_0} \sum_{i=\pm} f_i^s(\eta) s_i(x,y). \tag{4}$$

Here s_0 is the peak entropy density which is adjusted to reproduce the experimentally observed charged hadron multiplicities.

Similarly, the net baryon density profile can be constructed as

$$n_B(x,y,\eta;\tau_0) = \frac{1}{\tau_0} \sum_{i=\pm} f_i^{n_B}(\eta) s_i(x,y). \tag{5}$$

There is no additional normalization factor for the net baryon density because it is constrained by

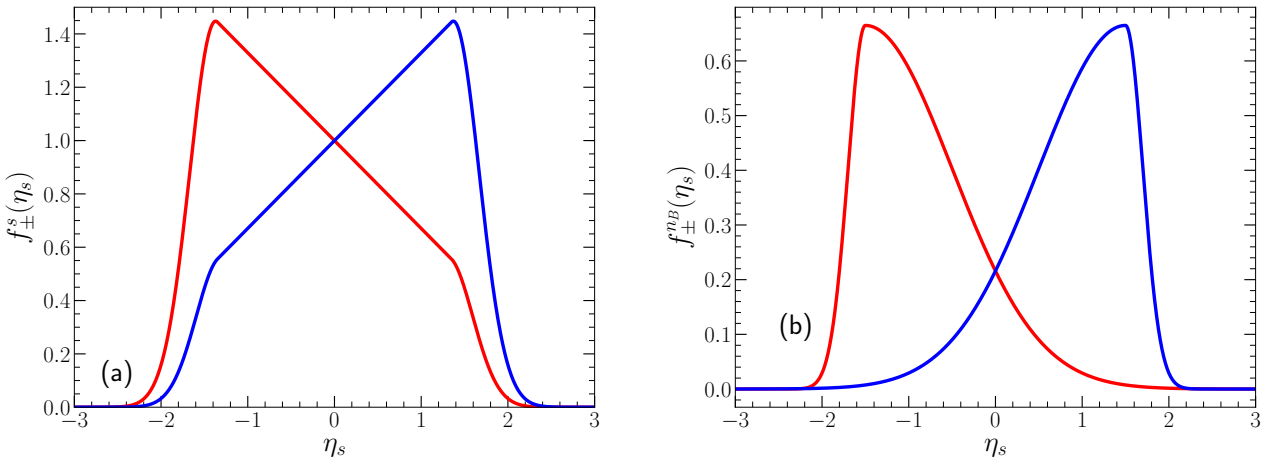

FIG. 1: Example of the envelope functions for entropy density and net baryon density $f^s_\pm(\eta_s)$ and $f^{n_B}_\pm(\eta_s)$ in Au+Au collisions at $\sqrt{s_{\rm NN}} = 19.6\,{\rm GeV}$.

the total number of participant nucleons $N_{\rm part}$, $\int \tau_0 dxdyd\eta n_B(x,y,\eta;\tau_0) = N_{\rm part}$. The envelope functions in Eqs. (4) and (5) are chosen as,

$$f^s_\pm(\eta) = \theta(\eta_{\rm max} - |\eta|)\left(1 \pm \frac{\eta}{\eta_{\rm max}}\right) \times \left[\theta(|\eta| - \eta^s_0)\exp\left(-\frac{(|\eta| - \eta^s_0)^2}{2\sigma^2_{\eta,s}}\right) + \theta(\eta^s_0 - |\eta|)\right] \quad (6)$$

where the maximum extension in space-time pseudo-rapidity $\eta_{\rm max}$ is chosen to be equal to the beam rapidity $y_{\rm beam} = {\rm arctanh}\left(\frac{\sqrt{\gamma_L^2-1}}{\gamma_L}\right)$ of incoming nucleons. The parameters η^s_0 and $\sigma_{\eta,s}$ are determined to reproduce the pseudo-rapidity distribution of charged hadrons $dN^{\rm ch}/d\eta$.

For the net baryon density envelope profile,

$$f^{n_B}_\pm(\eta) = \frac{1}{\mathcal{N}}\left[\theta(\eta - \eta^{n_B,\pm}_0)\exp\left(-\frac{(\eta - \eta^{n_B,\pm}_0)^2}{2\sigma^2_{\eta,\pm}}\right) + \theta(\eta^{n_B,\pm}_0 - \eta)\exp\left(-\frac{(\eta - \eta^{n_B,\pm}_0)^2}{2\sigma^2_{\eta,\mp}}\right)\right] \quad (7)$$

where $\mathcal{N}$ is the normalization of the envelope profile which ensures

$$\int d\eta f^{n_B}_\pm(\eta) = 1. \quad (8)$$

The peak position $\eta^{n_B,\pm}_0$ is determined by the measured rapidity loss in the net proton distribution and the width parameters $\sigma_{\eta,\pm}$ determine the shape of the final $dN^{p-\bar{p}}/dy$. Figure 1 shows an example of the η_s envelope functions for entropy density and net baryon density. The parameters in Eq. (6) were determined by comparing the pseudo-rapidity distribution of the charge hadron multiplicity with the PHOBOS measurement [28]. Because there is no measurements of the net proton rapidity distribution for Au+Au collisions at 19.6 GeV at the RHIC, we fixed the parameters in Eq. (7) by comparing the shape of net proton rapidity distribution measured in PbPb collisions at 17.3 GeV at SPS [29]. The values of these parameters are listed in Table I .

$\sqrt{s_{\rm NN}}$ (GeV)	$y_{\rm beam}$	τ_0 (fm)	s_0	η^s_0	$\sigma_{\eta,s}$	$\eta^{n_B}_0$	$\sigma_{\eta,+}$	$\sigma_{\eta,-}$
19.6	3.04	1.5	6.3	2.7	0.3	1.5	0.2	1.0

TABLE I: A list of parameters for MC-Glauber initial conditions for Au+Au collisions at 19.6 GeV.

B. Hydrodynamics at finite baryon density

The hydrodynamical equation of motion at finite net baryon density can be written as,

$$\partial_\mu T^{\mu\nu} = 0, \quad (9)$$

$$\partial_\mu J^\mu_B = 0, \quad (10)$$

where the system's energy momentum tensor can be decomposed as

$$T^{\mu\nu} = eu^\mu u^\nu - (P + \Pi)\Delta^{\mu\nu} + \pi^{\mu\nu}, \quad (11)$$

and

$$J^\mu_B = n_B u^\mu + q^\mu. \quad (12)$$

Here $\Delta^{\mu\nu} = g^{\mu\nu} - u^\mu u^\nu$ is a projection operator, u^μ is the flow velocity, and $g^{\mu\nu} = {\rm diag}(1,-1,-1,-1)$ is the space-time metric. The dissipative currents in the system

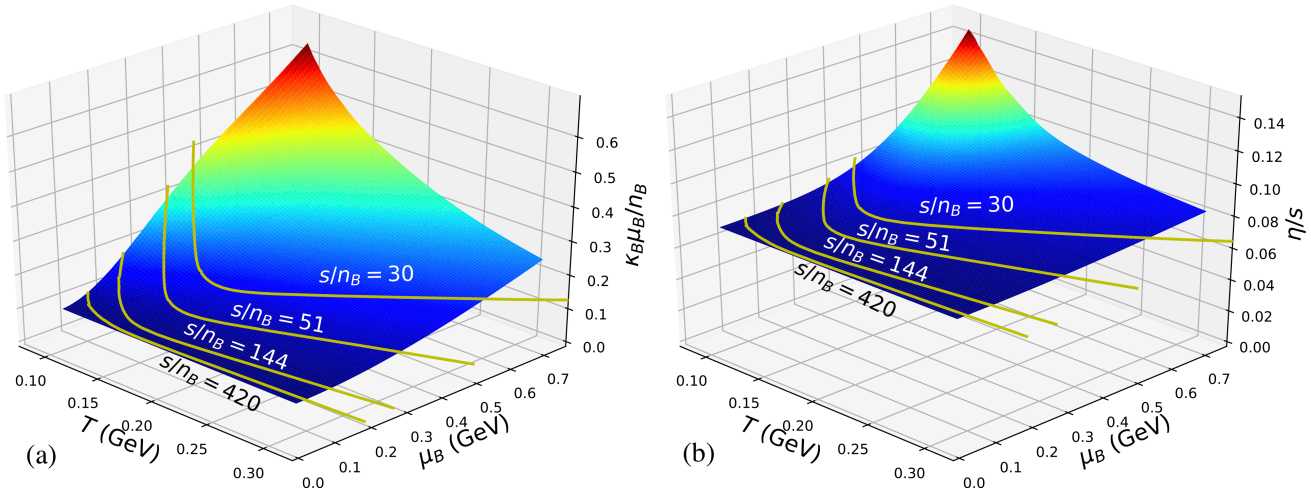

FIG. 2: The temperature and net baryon chemical potential dependence of the net baryon diffusion constant (a) and specific shear viscosity (b) for $C_B = 0.4$ and $C_\eta = 0.08$, respectively.

are the bulk viscous pressure Π, the net baryon diffusion current q^μ, and shear stress tensor $\pi^{\mu\nu}$. In this work, we consider only the effects of the shear stress tensor and net baryon diffusion. These two currents are described by the Israel-Stewart-like equations,

$$\Delta^{\mu\nu} D q_\nu = -\frac{1}{\tau_q}\left(q^\mu - \kappa_B \nabla^\mu \frac{\mu_B}{T}\right) - \frac{\delta_{qq}}{\tau_q} q^\mu \theta - \frac{\lambda_{qq}}{\tau_q} q_\nu \sigma^{\mu\nu} + \frac{l_{q\pi}}{\tau_q}\Delta^{\mu\nu}\partial_\lambda \pi^\lambda{}_\nu - \frac{\lambda_{q\pi}}{\tau_q}\pi^{\mu\nu}\nabla_\nu \frac{\mu_B}{T}, \tag{13}$$

and

$$\Delta^{\mu\nu}_{\alpha\beta} D \pi^{\alpha\beta} = -\frac{1}{\tau_\pi}(\pi^{\mu\nu} - 2\eta\sigma^{\mu\nu}) - \frac{\delta_{\pi\pi}}{\tau_\pi}\pi^{\mu\nu}\theta - \frac{\tau_{\pi\pi}}{\tau_\pi}\pi^{\lambda\langle\mu}\sigma^{\nu\rangle}{}_\lambda + \frac{\phi_7}{\tau_\pi}\pi^{\langle\mu}{}_\alpha \pi^{\nu\rangle\alpha} + \frac{l_{\pi q}}{\tau_\pi}\nabla^{\langle\mu} q^{\nu\rangle} + \frac{\lambda_{\pi q}}{\tau_\pi} q^{\langle\mu}\nabla^{\nu\rangle}\frac{\mu_B}{T}. \tag{14}$$

Here the evolution of the diffusion current is driven by the gradient of the net baryon chemical potential μ_B divided by temperature T. The thermodynamic force for the shear viscous pressure is the velocity shear tensor $\sigma^{\mu\nu} = \nabla^{\langle\mu} u^{\nu\rangle}$, and $A^{\langle\mu\nu\rangle} = \Delta^{\mu\nu}_{\alpha\beta} A^{\alpha\beta}$ projects out the part that is traceless and transverse to the flow velocity u_μ using the double, symmetric, and traceless projection operator, $\Delta^{\mu\nu}_{\alpha\beta} = \frac{1}{2}\left[\Delta^\mu_\alpha\Delta^\nu_\beta + \Delta^\nu_\alpha\Delta^\mu_\beta - \frac{2}{3}\Delta^{\mu\nu}_{\alpha\beta}\right]$. The system's expansion rate is $\theta = \partial_\mu u^\mu + u^\tau/\tau$.

The transport coefficients η and the baryon diffusion constant κ_B are chosen as

$$\frac{\eta T}{e+\mathcal{P}} = C_\eta \tag{15}$$

and

$$\kappa_B = \frac{C_B}{T} n_B \left(\frac{1}{3}\coth\left(\frac{\mu_B}{T}\right) - \frac{n_B T}{e+\mathcal{P}}\right). \tag{16}$$

The specific shear viscosity is chosen to be $C_\eta = 0.08$. The constant coefficient C_B will be varied to study the effect of the net baryon diffusion. The T and μ_B dependence of κ_B in Eq. (16) is derived from the Boltzmann equation in the relaxation time approximation (see Appendix A). We show the dimensionless quantity $\kappa_B\mu_B/n_B$ along with η/s as functions of T and μ_B in Fig. 2. Four lines of constant s/n_B, that reflect the averaged values realized in Au+Au collisions at $\sqrt{s_{\rm NN}} = 200, 62.4, 19.6$, and 14.5 GeV, demonstrate what values of the transport parameters typically contribute.

τ_q	δ_{qq}	λ_{qq}	$l_{q\pi}$	$\lambda_{q\pi}$	
$\frac{C_B}{T}$	τ_q	$\frac{3}{5}\tau_q$	0	0	
τ_π	$\delta_{\pi\pi}$	$\tau_{\pi\pi}$	ϕ_7	$l_{\pi q}$	$\lambda_{\pi q}$
$\frac{5C_\eta}{T}$	$\frac{4}{3}\tau_\pi$	$\frac{10}{7}\tau_\pi$	$\frac{9}{70}\frac{4}{\varepsilon+\mathcal{P}}$	0	0

TABLE II: A list for the second order transport coefficients used in the evolution equations for the net baryon diffusion current q^μ and the shear stress tensor $\pi^{\mu\nu}$.

Table II summarizes the choice of the second order transport coefficients used in Eqs. (13) and (14). The expression for the baryon diffusion relaxation time, τ_q is chosen to be proportional to $1/T$ (as it is exactly in a conformal system), with the proportionality constant C_B a free parameter. The remaining transport coefficients listed in the table are from calculations assuming kinetic theory in the massless limit [30–33]. Recent calculations of transport coefficients taking into account a finite (and thermal) mass, were performed in Ref. [34].

The system of hydrodynamic equations (9) and (10) needs to be closed with the equation of state (EoS) of the fluid. In this work, the EoS of the QCD matter is constructed using lattice QCD calculations [36, 37]. We consider a crossover-type EoS and leave implementa-

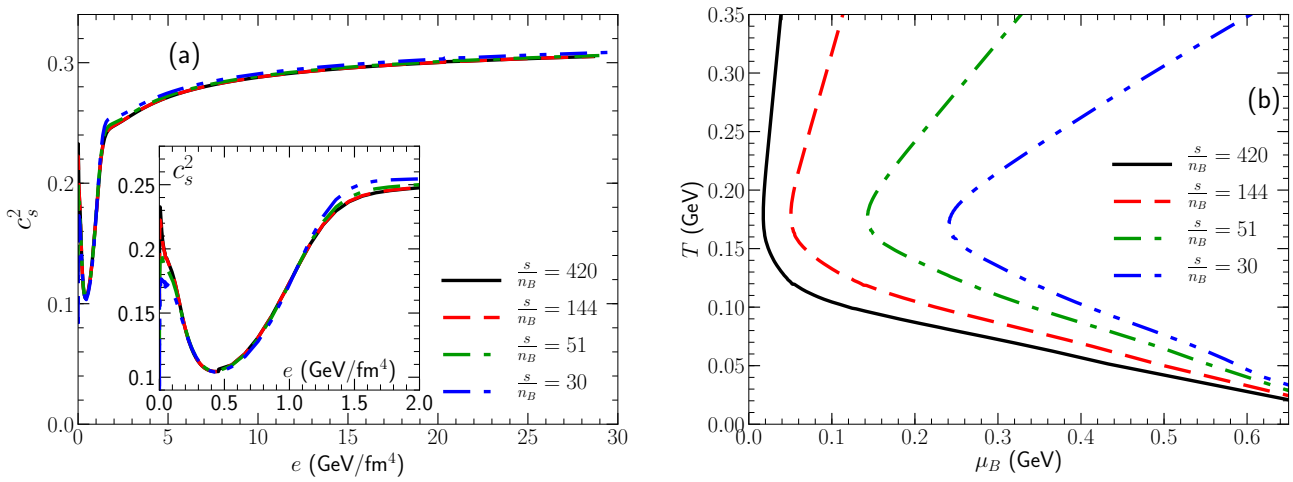

FIG. 3: *Panel (a)*: The square of the speed of sound as a function of the local energy density along constant s/n_B lines. *Panel (b)*: Temperature as a function of net baryon chemical potential along constant s/n_B lines. The collision energies correspond to these s/n_B lines (from top down in the legend) are $\sqrt{s_{\rm NN}} = 200, 62.4, 19.6$, and 14.5 GeV according to Ref. [35].

tion of the QCD critical point for future study. At zero baryon chemical potential, the pressure of the system is computed as a function of the local temperature via [38],

$$\frac{\mathcal{P}(T)}{T^4} = \frac{\mathcal{P}(T_{\rm low})}{T_{\rm low}^4} + \int_{T_{\rm low}}^{T} \frac{dT'}{T'} \frac{e-3\mathcal{P}}{T'^4}, \tag{17}$$

where the trace anomaly $e-3\mathcal{P}$ is computed from lattice QCD as a function of temperature. The lower integration limit $T_{\rm low}$ is chosen to be sufficiently small such that $\mathcal{P}(T_{\rm low})$ can be neglected because of the exponential suppression. Since of the sign problem, it is not possible to directly calculate the EoS at finite baryon density using lattice QCD. Instead, the μ_B dependence of the EoS is constructed using the following Taylor expansion,

$$\frac{\mathcal{P}(T,\mu_B)}{T^4} = \frac{\mathcal{P}(T)}{T^4}\bigg|_{\mu_B=0} + c_2(T)\left(\frac{\mu_B}{T}\right)^2 + c_4(T)\left(\frac{\mu_B}{T}\right)^4 + \mathcal{O}\left(\left(\frac{\mu_B}{T}\right)^6\right), \tag{18}$$

where $c_2(T)$ and $c_4(T)$ are the expansion coefficients. The former coefficient is extracted using lattice QCD susceptibility calculations [37] while the latter follows from ratios of the second and fourth order susceptibilities, computed hadron resonance and parton gas pictures. It is noteworthy that the lattice QCD EoS and baryon susceptibilities are known to agree with those of the resonance gas slightly below the crossover. For temperatures below the transition temperature $T_{\rm trans}(\mu_B)$, the lattice QCD EoS is smoothly matched to the hadron resonance gas EoS because the Taylor expansion is not well defined at lower T and energy, momentum, and net baryon number need to be conserved at the Cooper-Frye freeze-out [39]:

$$\frac{\mathcal{P}}{T^4} = \frac{1}{2}\left(1-\tanh\frac{T-T_{\rm trans}}{\Delta T_{\rm trans}}\right)\frac{\mathcal{P}_{\rm HRS}(T,\mu_B)}{T^4} + \frac{1}{2}\left(1+\tanh\frac{T-T_{\rm trans}}{\Delta T_{\rm trans}}\right)\frac{\mathcal{P}_{\rm lat}(T_s,\mu_B)}{T_s^4}. \tag{19}$$

For the transition temperature of the two EoS, we use the ansatz $T_{\rm trans}(\mu_B) = 0.166$ GeV $- 0.4(0.139$ GeV$^{-1}\mu_B^2 + 0.053$ GeV$^{-3}\mu_B^4)$ motivated by a chemical freeze-out curve [40]. The shift $T_s = T + 0.4[T_{\rm trans}(0) - T_{\rm trans}(\mu_B)]$ is introduced to ensure that thermodynamic variables are increasing functions of T and μ_B at very large baryon chemical potential, and should not affect much the bulk dynamics. The entropy density, the net baryon number, and the energy density can be obtained from the thermodynamic relations $s = \partial\mathcal{P}/\partial T|_{\mu_B}$, $n_B = \partial\mathcal{P}/\partial\mu_B|_T$, and $e = Ts - \mathcal{P} + \mu_B n_B$. The speed of sound squared at the finite μ_B is computed as

$$c_s^2(e,n_B) = \frac{\partial\mathcal{P}}{\partial e}\bigg|_{n_B} + \frac{n_B}{(e+\mathcal{P})}\frac{\partial\mathcal{P}}{\partial n_B}\bigg|_e. \tag{20}$$

To see whether we should expect a large effect on the collision dynamics from the finite μ_B values present in smaller energy collisions, in Fig. 3a we plot c_s^2 as a function of local energy density for several constant s/n_B values. From $\sqrt{s_{\rm NN}} = 14.5$ to $\sqrt{s_{\rm NN}} = 200$ GeV, the square of the speed of sound does not change significantly. The constant s/n_B trajectories are shown in the $T-\mu_B$ plane in Fig. 3b.

In Appendix C we present several validation studies of our 3+1D numerical hydrodynamic implementation at finite baryon density.

C. Particlization and hadronic cascade

As the temperature drops in the hadronic phase, we convert the macroscopic fluid cells into particle samples via the Cooper-Frye procedure [41]. At finite μ_B, we choose to perform the Cooper-Frye conversion on a constant switching energy density hyper-surface, $e_{\rm sw} = 0.4$ GeV/fm^3. This is because the chosen constant energy density line in the $T-\mu_B$ plane follows very well the chemical freeze-out points extracted from the thermal fits done by the STAR Collaboration [4]. This is demonstrated in Fig. 4, where we vary $e_{\rm sw}$.

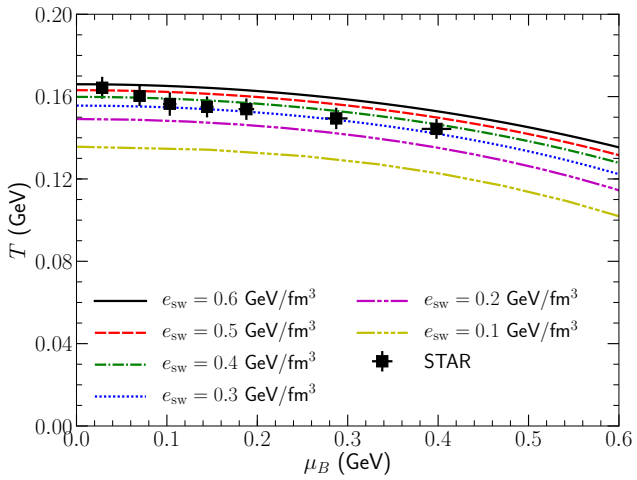

FIG. 4: Constant energy density freeze-out lines compared with the extracted chemical freeze-out points from the STAR collaborations [4].

Because of the long overlapping time at low collision energies, one would have expected that non-negligible amount of matter had already flown out of the switching hyper-surface before the hydrodynamic simulation starts. This is usually referred to as "corona". We define the corona as those cells whose local energy densities are between 0.05 GeV/fm^3 and $e_{sw} = 0.4$ GeV/fm^3. We use the Cooper-Frye formula to convert these corona fluid cells to particles at the first time step of the hydrodynamic evolution and then feed them into the hadronic transport simulation. Because there is no transverse flow velocity at the starting time of the hydrodynamic simulations, these corona particles are emitted isotropically according to their local thermal equilibrium distributions. The effect of the corona on hadronic flow observables will be discussed in the next section.

The momentum distribution of thermally emitted particles from one fluid cell is,

$$E\frac{d^3N_i}{d^3p} = \frac{g_i}{(2\pi)^3}p^\mu\Delta^3\sigma_\mu\Big(f_i^{\rm eq}(E,T,\mu_B) + \delta f_i^{\rm shear}(E,T,\mu_B,\pi^{\mu\nu}) + \delta f_i^{\rm diffusion}(E,T,\mu_B,q^\mu)\Big)\Big|_{E=p\cdot u}, \quad (21)$$

where the $\delta f^{\rm shear}$ and $\delta f^{\rm diffusion}$ are the out-of-equilibrium corrections from shear viscosity and net baryon diffusion. As in previous work [42] we employ

$$\delta f_i^{\rm shear} = f_i^{\rm eq}(x,p)(1\pm f_i^{\rm eq}(x,p))\frac{p^\mu p^\nu \pi_{\mu\nu}}{2T^2(e+P)}. \quad (22)$$

In the relaxation time approximation, the net baryon diffusion $\delta f^{\rm diffusion}$ for a single species of particle i is [43, 44]

$$\delta f_i^{\rm diffusion}(x,p) = f_i^{\rm eq}(x,p)(1\pm f_i^{\rm eq}(x,p)) \times\left(\frac{n_B}{e+\mathcal{P}}-\frac{b_i}{E}\right)\frac{p^{\langle\mu\rangle}q_\mu}{\hat\kappa_B}, \quad (23)$$

where b_i is the baryon number of particle species i, $p^{\langle\mu\rangle}=\Delta^{\mu\nu}p_\nu$, and the transport coefficient $\hat\kappa_B$ is defined in Appendix A. An alternative form of diffusion out-of-equilibrium correction was recently derived using the 14-moment method [45]. We note that $\delta f_i^{\rm diffusion}$ is non-zero even for mesons (that have zero baryon number). This is because the changes in the baryon chemical potential can lead to variations in the thermal pressure, which will change the momentum distributions of mesons. Using Eq. (21) the system's total net baryon number can be computed as

$$\begin{aligned} N^B - N^{\bar B} &= \int d^3\sigma_\mu \sum_i g_i b_i \\ &\quad\times\int_p p^\mu(f_i^{\rm eq}+\delta f_i^{\rm shear}+\delta f_i^{\rm diffusion}) \\ &= \int d^3\sigma_\mu (n_B u^\mu + q^\mu)\,, \end{aligned} \quad (24)$$

where $\int_p = \int\frac{d^3p}{E(2\pi)^3}$. Because the hydrodynamic equation solves $\partial_\mu(n_Bu^\mu+q^\mu)=0$, the net baryon number is conserved during the hydrodynamic evolution as well as on the conversion surface before and after the conversion. The inclusion of $\delta f_i^{\rm diffusion}$ in the Cooper-Frye formula takes into account contributions from the diffusion current q^μ in Eq. (24) and is essential to ensure the conservation of net baryon number during the conversion from fluid cells to particles.

In this work, we generalized the publicly available numerical code iSS[2] to perform the particlization simulations. Detailed implementation and cross checks for the numerical procedure are discussed in Appendix B.

After the particle conversion, we feed particles into hadronic cascade models, such as UrQMD [46, 47] and JAM[3] [48], to simulate the transport dynamics in the dilute hadronic phase.

---

[2] The latest version of the code package can be downloaded from https://github.com/chunshen1987/iSS.

[3] The latest version of JAM can be downloaded from http://www.aiu.ac.jp/~ynara/jam/

III. COLLECTIVITY IN AU+AU COLLISIONS AT RHIC BES ENERGIES

We will focus our study of hadronic flow observables on central and semi-peripheral Au+Au collisions at 19.6 GeV. At this collision energy, the baryon chemical potential can reach up to ∼200 MeV in the mid-rapidity region. Consequently, we expect the net baryon current and its diffusion to have sizeable effects on the hadronic flow observables near the mid-rapidity region which can be measured by the STAR experiments.

A. Hydrodynamical evolution with net baryon diffusion

Based on the hydrodynamic equations of motion, the net baryon diffusion current only directly affects the evolution of the net baryon density. Nevertheless, it modifies the system's energy density and flow velocity evolution indirectly, via the modification of the pressure $\mathcal{P}(e, n_B)$, given by the equation of state. Thus we expect this dissipative current to have less influence on the system's evolution compared to the usual dissipative effects due to shear and bulk viscosities.

To understand the effect of net baryon diffusion on hadronic flow observables, it is instructive to study the time evolution of μ_B/T, whose spatial gradients are the thermal dynamic force of the net baryon diffusion current, q^μ.

Figure 5 shows the time evolution of μ_B/T along the longitudinal and transverse directions. At the starting time of the hydrodynamic simulation, the ratio μ_B/T peaks around $\eta_s = \pm 1.5$. The gradients of μ_B/T dominantly point to the mid-rapidity region. Thus the baryon diffusion current will transport more baryons from forward rapidities to the central rapidity region. We also find that the value of μ_B/T increases in dilute energy density regions in both very forward rapidity and in towards the edges in the transverse plane. Such a distribution leads to the spatial gradients of μ_B/T pointing opposite to the pressure gradients. From these observations in the longitudinal and transverse directions, we expect that the net baryon diffusion current q^μ will act against the hydrodynamic flow, and will reduce the net baryon flow coefficients.

B. Effects of baryon diffusion on observables

In this section, we study how baryon diffusion in the hydrodynamic simulations affects various experimental observables. We vary the amount of diffusion by tuning the value of the pre-factor C_B in Eq. (16).

Figure 6a shows the rapidity distribution of produced hadrons in the top 0-5% central Au+Au collisions at $\sqrt{s}$ =19.6 GeV. The system's total entropy is tuned to

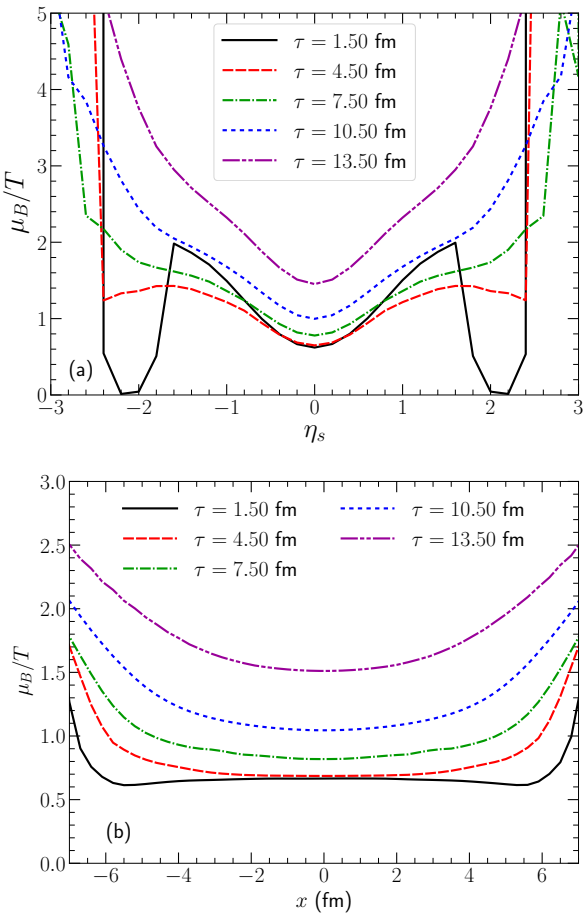

FIG. 5: Time evolution of the μ_B/T along longitudinal direction for points at $x = 0$ and $y = 0$ (panel (a)) and transverse plane along $y = 0$ and $\eta_s = 0$ (panel (b)).

reproduce the positive pion yield at mid-rapidity, measured by the STAR collaboration [4]. The rapidity envelope profile is tuned to reproduce the rapidity dependence measured by the PHOBOS collaboration [28]. The charged hadron multiplicity is slightly overestimated mainly because the PHOBOS measurement is for the 0-6% centrality. The net baryon diffusion has negligible effect on mesons and charged hadrons.

In Fig. 6b we demonstrate that the rapidity dependence of net protons is sensitive to the magnitude of the baryon diffusion coefficient. As discussed in Sec. III A , the baryon diffusion current is driven by gradients of μ_B/T, which transports net baryons from forward rapidity to the mid-rapidity region. This effect is visibly stronger for larger C_B.

Unfortunately, the measured shape of the net proton rapidity distribution cannot be used to constrain the amount of net baryon diffusion, because of the theoretical uncertainties in determining the initial baryon stopping. This is explicitly demonstrated in Fig. 7a, where we have adjusted the initial baryon rapidity distribution for given values of C_B. This shows that approximately the same

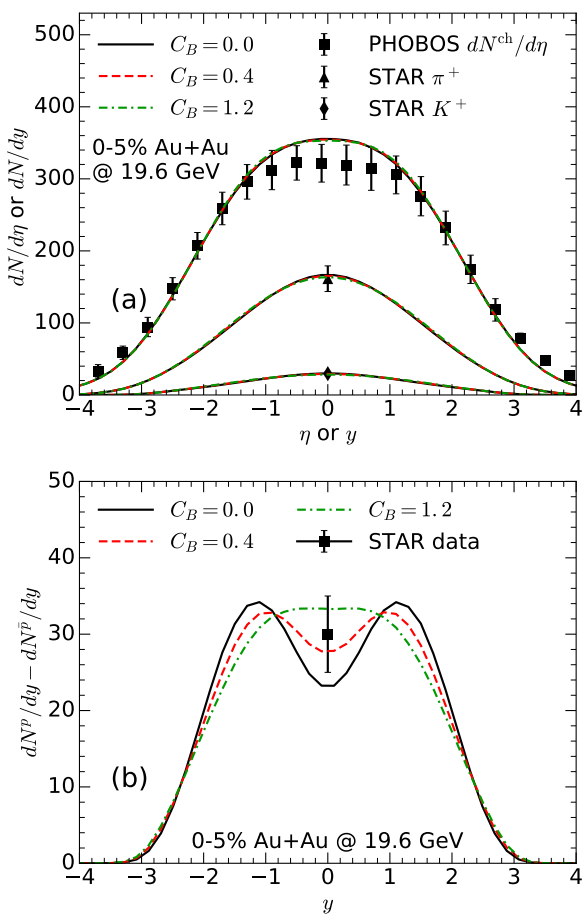

FIG. 6: *Panel (a)*: The pseudo-rapidity and rapidity distributions of the charged hadron, identified π^+, and K^+ compared to the PHOBOS and STAR measurements in 0-5% Au+Au collisions at 19.6 GeV[4, 28]. *Panel (b)*: The net proton rapidity distribution with different choices of the net baryon diffusion constant compared with the STAR measurements.

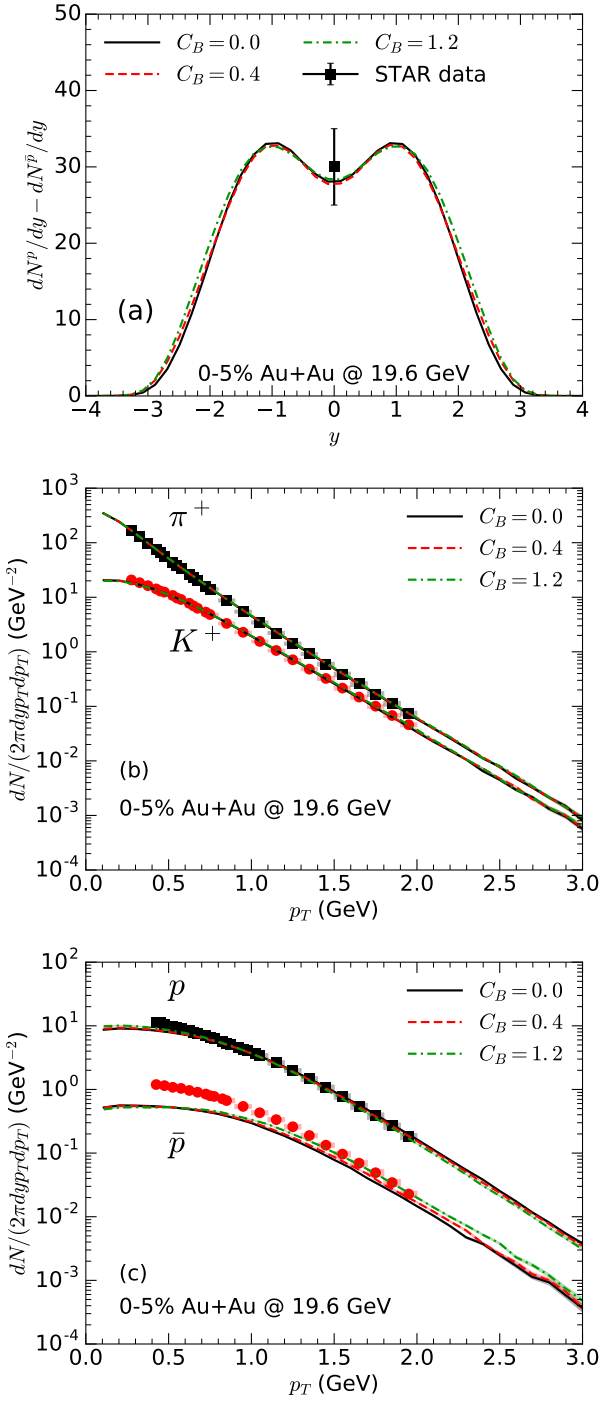

FIG. 7: *Panel (a)*: The fit of the net proton rapidity distribution with different choices of the net baryon diffusion constant in the simulations. *Panel (b)*: The single particle spectra of π^+ and K^+ with different choices of the net baryon diffusion constant. *Panel (c)*: The single particle spectra of proton and anti-proton with different choices of the net baryon diffusion constant.

final distribution is obtained for largely different baryon diffusion currents.

It is possible to find further constraints by considering both experimental data sensitive to longitudinal and transverse dynamics simultaneously. For a given C_B, the initial condition can be constrained by the net proton rapidity distribution as above, and studying the transverse dynamics of the collision system could then be used to distinguish different C_B values.

Figures 7b and 7c show transverse momentum spectra of identified particles. The p_T-spectra of light mesons, such as π^+ and K^+, are insensitive to the net baryon diffusion as expected. Proton and anti-proton spectra obtained using different degrees of net baryon diffusion are compared in Fig. 7c. The effect of the net baryon diffusion constant C_B looks small in the plot. To better quantify the effect, we compare the difference in the average transverse momentum of protons and anti-protons. The result is shown in Table III for different choices of C_B.

The hydrodynamic simulation produces a slightly larger mean-p_T for anti-protons than for protons. This

	$C_B = 0.0$	$C_B = 0.4$	$C_B = 1.2$
$\langle p_T \rangle(\bar{p}) - \langle p_T \rangle(p)$ (GeV)	0.049(2)	0.079(2)	0.134(2)
$\langle p_T \rangle(\bar{p}) - \langle p_T \rangle(p)$ (GeV) (no diffusion δf)	0.049(2)	0.050(2)	0.056(2)

TABLE III: The difference of the averaged transverse momentum between anti-protons and protons at different values of the net baryon diffusion constant C_B. The associated statistical errors are quoted using parenthesis.

difference grows with increasing net baryon diffusion. Part of this effect is caused by the diffusive evolution, because the μ_B/T gradient in the transverse plane tends to diffuse net baryon number into the central region where the radial flow is relatively smaller. An even larger contribution to the mean-p_T difference is due to the baryon diffusion δf corrections to the baryon spectra. We will discuss this effect in more detail in the next section.

In Fig. 8 we show the transverse momentum elliptic flow coefficient v_2 for positive pions (panel a), protons (b), and anti-protons (c). As for the transverse momentum spectra, pion v_2 does not change within statistical errors with the value of C_B. For protons and anti-protons we find a sizeable and opposite effect: Proton v_2 decreases with increasing C_B, while anti-proton v_2 increases. We will show in the following section that the differences are to a large part generated by off-equilibrium corrections to the distribution functions.

We find that the net baryon diffusion has a small influence on the system's transverse dynamics, such as the hydrodynamic flow pattern. The major effects to the baryonic observables are coming from the off-equilibrium corrections at the freeze-out stage. Because of this, baryon diffusion cannot be constrained quantitatively from experimental data in our current analyses.

It should be noted that unlike the other particle species, $\bar{p}$ is not well described for any C_B. We expect that it should be possible to improve the agreement by fine tuning both the initial entropy and net-baryon distributions, as well as the switching energy density.

C. The effects of the out-of-equilibrium corrections from net baryon diffusion

Figure 9 shows the effect of the out-of-equilibrium corrections to the particle distributions on net proton rapidity spectra. We show separately the effect from shear viscous corrections and baryon diffusion corrections. The δf correction from the net baryon diffusion current reduces the net proton yield. As we discussed in Sec. II C, this δf correction is essential to conserve the total net baryon number during the Cooper-Frye conversion procedure.

Please note that a non-zero net baryon diffusion current on the freeze-out surface modifies identified particle yields as shown in Eq. (B10) in Appendix B. Thus, the non-equilibrium evolution of the baryon diffusion current

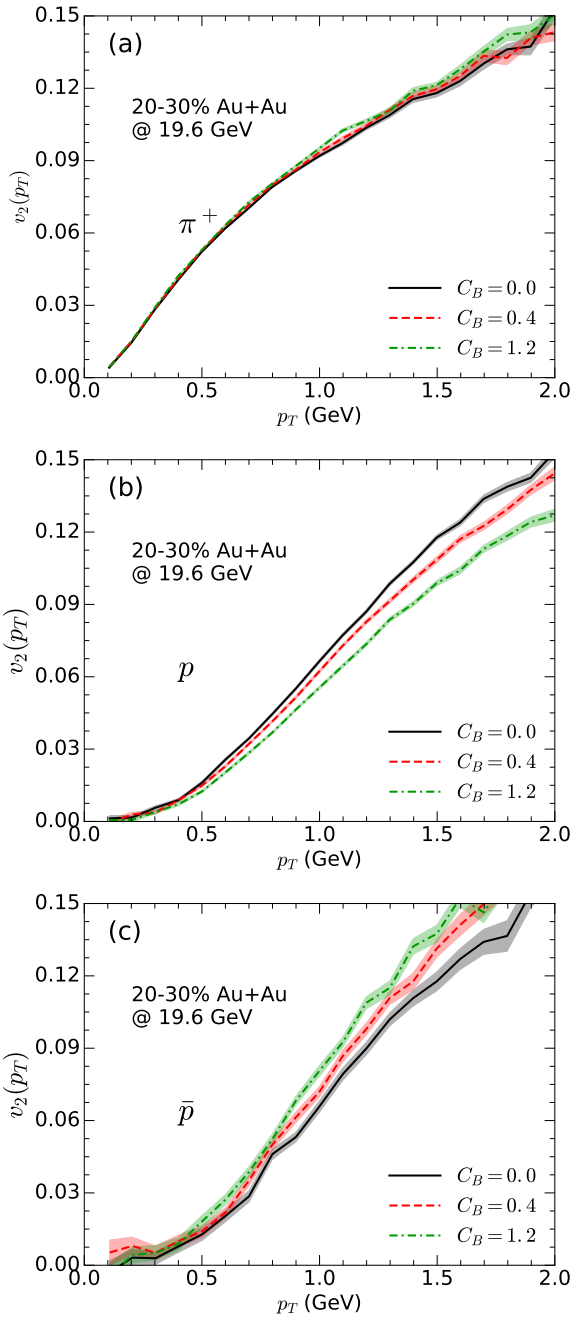

FIG. 8: The p_T-differential elliptic flow coefficients of identified π^+ (panel (a)), p (panel (b)), and $\bar{p}$ (panel (c)) with different net baryon diffusion constants in the hydrodynamic simulations for 20-30% Au+Au collisions at 19.6 GeV. The shaded bands indicate statistical errors.

will give corrections the chemical freeze-out parameters determined in thermal model fits [4]. Because the baryon diffusion δf reduces the net proton yield, the averaged chemical potential on the freeze-out surface is about 30 MeV larger with baryon diffusion compared to the simulations without diffusion.

In Fig. 10 we show identified particle spectra and their

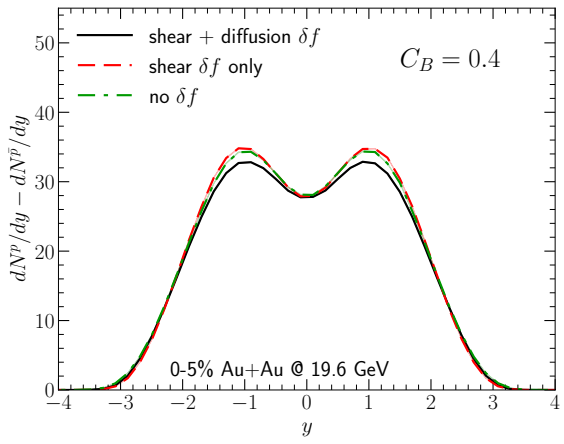

FIG. 9: The effects of the out-of-equilibrium corrections δf from shear viscosity and net baryon number diffusion on the net proton rapidity distribution.

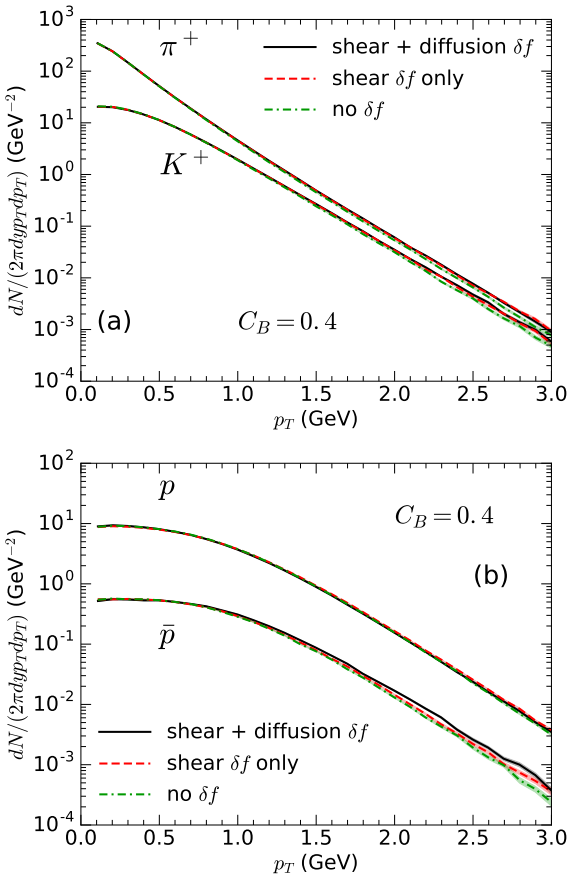

FIG. 10: The correction of shear and net baryon diffusion δf to the transverse momentum spectra of π^+, K^+, p, and $\bar{p}$ at the mid-rapidity in the hybrid simulations.

dependence on shear and baryon diffusion δf corrections. For all species the effects are small, with the largest difference visible for anti-protons at $p_T > 2$ GeV.

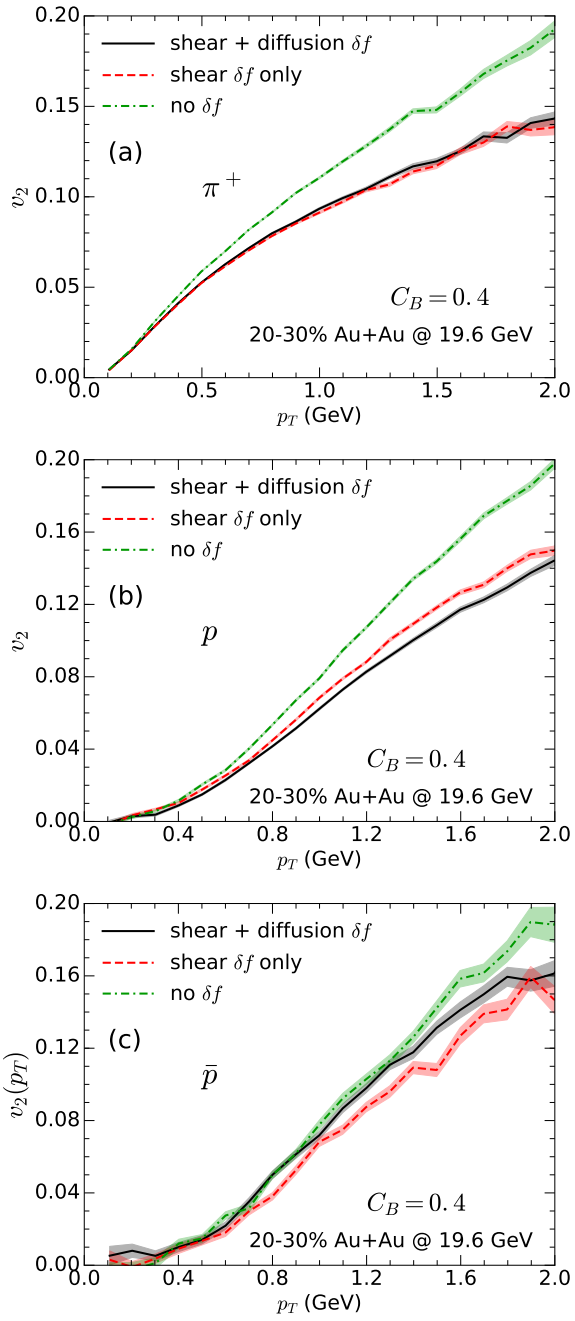

FIG. 11: The correction of shear and net baryon diffusion δf to the p_T-differential v_2 of π^+, p, and $\bar{p}$ in hybrid simulations. The shaded bands indicate statistical errors.

Figure 11 shows the effect of both δf corrections on the elliptic flow of pions (a), protons (b), and anti-protons (c). The shear δf leads to the typical reduction of v_2 for all particle species. Its effects on particle p_T-differential v_2 is larger than the one from the baryon diffusion. Because the baryon diffusion δf depends on the baryon charge of the particle species, it reduces proton v_2 more but increases anti-proton v_2. It enhanced the difference between proton and antiproton $v_2(p_T)$.

D. Effects of hadronic afterburner at BES energies

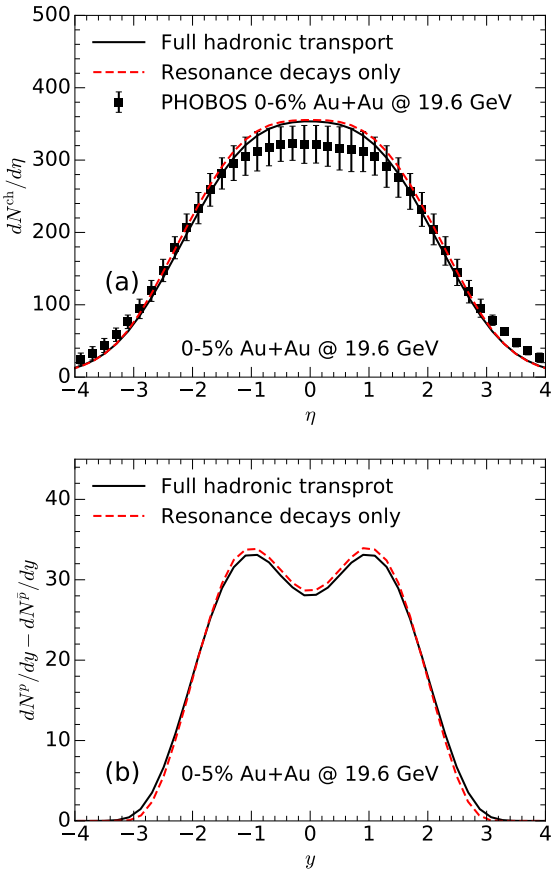

FIG. 12: The effects of hadronic rescatterings on charged hadron (a) and net proton (b) rapidity distribution.

Figure 12 shows the effect of hadronic rescatterings on the rapidity distributions of identified particles. The late hadronic rescattering phase has a small effect on the shape of the rapidity distribution of charged hadrons. The net protons rapidity distribution is slightly widened by scatterings with other hadrons.

As in Table III, the mean transverse momentum of anti-protons is slightly larger than the proton mean p_T even without diffusion at $C_B = 0$. Table IV studies the origin of this difference in detail. Starting with thermally emitted protons and anti-protons from the Cooper-Frye conversion surface, the anti-proton $\langle p_T \rangle$ is only 11 MeV larger than that of the protons. This small difference can be understood by studying the time dependence of μ_B/T and the flow velocity u^τ on the hypersurface. The value of μ_B/T decreases by $\sim 10\%$ during the first 4 fm of the hydrodynamic evolution while the radial flow is building up. This anti-correlation between the time evolution of μ_B/T and u^τ at early times results in relatively more protons produced when the radial flow is small. The thermal production yields of both protons and anti-protons are small during the first 4 fm of the evolution. Thus, the difference in mean p_T is merely 11 MeV.

The hadronic corona (see Section II C) produces more protons than anti-protons near the edge of the fireball at the beginning of the hydrodynamic evolution. Because there is no hydrodynamic flow yet and the temperatures of the fluid cells are low, including these particles is expected to reduce the mean p_T. Indeed, we found that the proton mean p_T in Table IV is reduced twice as much as that of the antiproton when including this contribution.

The resonance feed down contribution from heavy excited baryon states reduces both proton and anti-proton mean p_T similarly. The slight reduction could be attributed to the fact that the shape of heavier particle spectra are less affected by the chemical potential and thus the particle-anti-particle difference in the mean p_T is smaller. Finally, the hadronic rescatterings among light mesons and baryons largely blue-shift proton and anti-proton mean p_T. Overall, hadronic rescatterings affect anti-protons more compared to protons. This is because a larger fraction of protons is produced at early times and in the dilute region (compared to anti-protons) and these protons scatter less. In summary, Table IV shows that the mean p_T difference between protons and anti-protons mainly originates from the late stage hadronic rescatterings. Note however, that the other differences in their production, discussed above, are necessary for the rescatterings to have this effect.

Figure 13 studies the effect of hadronic transport on particle p_T spectra. The Monte-Carlo results without hadronic rescatterings from the hadronic transport approach are also cross checked with the direct numerical calculations of Cooper-Frye freeze-out and resonance decays. Consistent results are found from the two independent approaches which validates the Monte-Carlo simulations. By comparing feed-down only pion spectra with the results from the full UrQMD simulation, we find that the additional scatterings in the hadronic phase flatten the pion spectra at high p_T.

Significant modifications on the shape of proton and anti-proton p_T-spectra are found in Fig. 13b. Both proton and anti-proton spectra get large blue-shifts because of scatterings with light mesons in the hadronic phase. We checked that in this baryon-rich environment the $B\bar{B}$ annihilation processes in the hadronic phase do not have an effect.

We conclude that at BES collision energies the hadronic transport phase is critical for baryon and anti-baryon spectra.

In Fig. 14 we investigate the effect of the hadronic transport phase on the identified particle p_T-differential elliptic flow coefficient. Firstly, consistent results are found between the Monte-Carlo approach (without rescatterings) and the direct numerical calculations of resonance decays. Unlike the minor modifications on the pion p_T spectra, the elliptic flow $v_2(p_T)$ of pions receives a sizable increase from the hadronic rescattering. This can be explained by the hadronic transport converting the remaining spatial eccentricity to particles' momen-

	$\langle p_T \rangle(p)$ (GeV)	$\langle p_T \rangle(\bar{p})$ (GeV)	$\langle p_T \rangle(\bar{p}) - \langle p_T \rangle(p)$ (GeV)
Thermal	0.758	0.769	0.011
Thermal + Corona	0.753	0.766	0.013
Thermal + Corona + resonances feed down	0.712	0.722	0.010
Thermal + Corona + full UrQMD	0.8748(4)	0.924(2)	0.049(2)

TABLE IV: The averaged transverse momentum of protons and anti-protons and their difference at different values from different effects in the hadronic phase. The results in the first three row were computed directly from the Cooper-Frye formula. There is no statistical error associated with them. The statistical errors for the results in the last row are quoted using parenthesis.

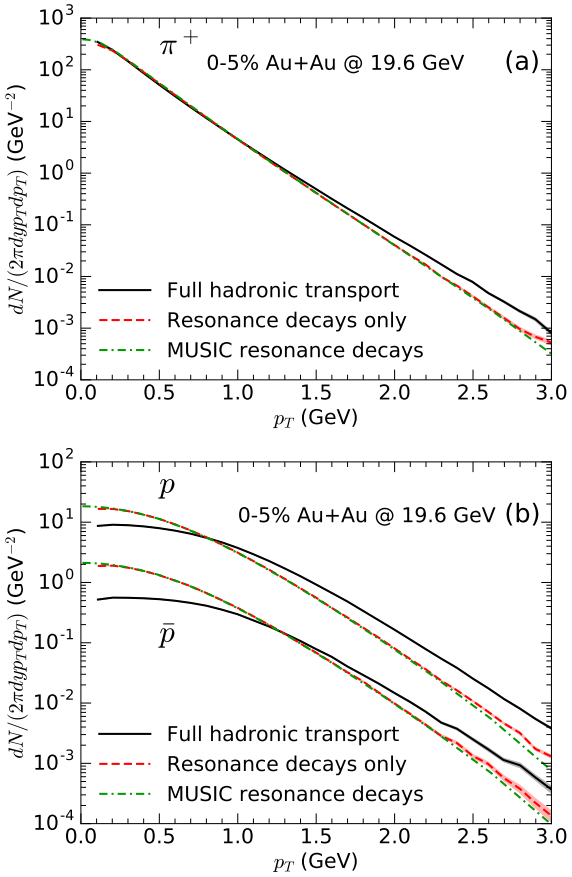

FIG. 13: The effects of hadronic transport on the transverse momentum spectra of final π^+, K^+ (a), p, and $\bar{p}$ (b).

tum anisotropy. Similar to pions, the high p_T (anti-)proton v_2 is increased owing to the additional lifetime of the system which converts more spatial eccentricity to momentum anisotropy. Meanwhile, the low p_T proton v_2 is reduced. This can be understood as a blue-shift effect, consistent with the modification of the proton spectra.

IV. CONCLUSIONS

The theoretical description of heavy ion collisions over a wide range of collision energies requires detailed fluid dynamic simulations with various complications appearing with lower energies. In this work we have introduced and studied the effects of net baryon diffusion that is expected to be present whenever the net baryon density is non-negligible. We have extended the 3+1 dimensional hydrodynamic simulation MUSIC to include baryon diffusion currents and analyzed its effects on a variety of observables in a simplified setup using smooth initial conditions.

Employing an equation of state at finite μ_B constructed from lattice QCD data and a hadron resonance gas, we were able to evolve systems with non-negligible net baryon density. We found that baryon diffusion, following the gradients of μ_B/T in the system, tends to transport net baryon number towards mid-rapidity.

While pions and kaons are not affected within the accuracy of the simulation, measurable effects on proton and anti-proton spectra and elliptic flow coefficients are present. In particular, the difference between proton mean transverse momentum and anti-proton mean transverse momentum increases with increasing baryon diffusion. Furthermore, baryon diffusion decreases proton elliptic flow while increasing anti-proton elliptic flow.

We have also shown that the hadronic microscopic transport stage is very important for baryon spectra and differential elliptic flow coefficients, primarily because of the additional blue-shift given to protons and anti-protons. Apart from this effect, it also continues the conversion from spatial to momentum anisotropy, an effect relevant also for pion elliptic flow.

Finally, we have identified the contributions to the difference in proton- and anti-proton $\langle p_T \rangle$, with the main effect coming from the hadronic afterburner. For the afterburner to have an effect it is also important where and when protons are produced relative to anti-protons, which depends on the distribution of μ_B on the freeze-out surface.

We have presented one important step towards the development of a comprehensive simulation of heavy ion collision dynamics relevant for collisions in the RHIC BES and BES II as well as the NA61/SHINE program. In the future it will be combined with other important developments in this direction, including a dynamical fluctuating initial state, hydrodynamic fluctuations, and multiple conserved currents with coupled diffusion coefficients [49], to result in a powerful theoretical tool that

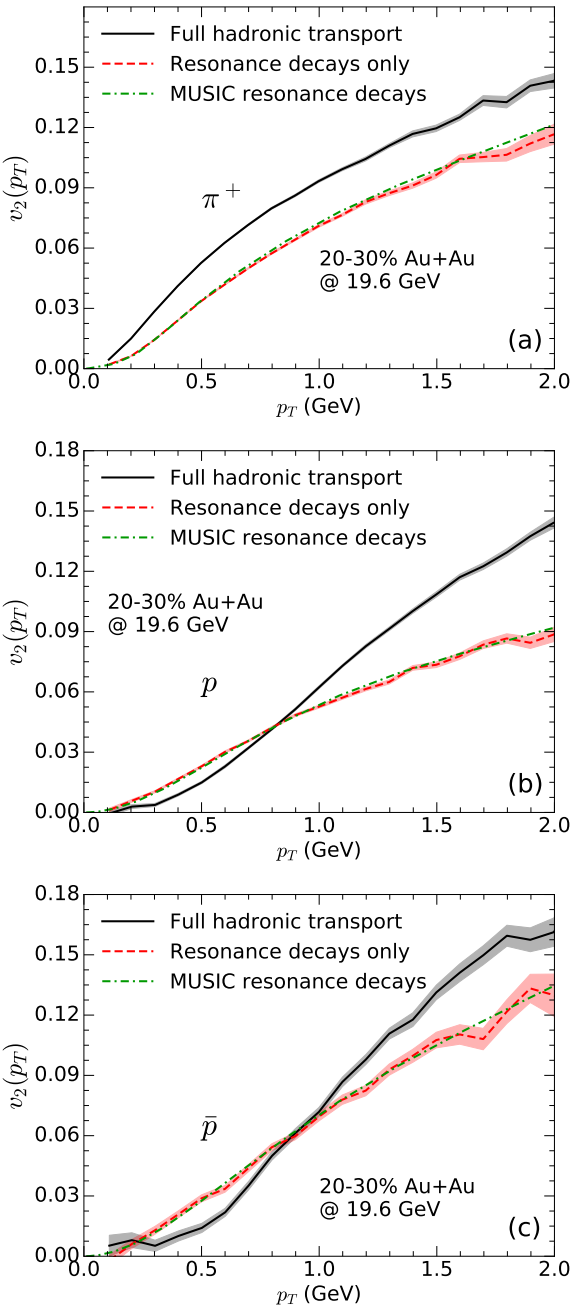

FIG. 14: The effects of hadronic transport on the differential v_2 of final π^+ (a), p (b), and $\bar{p}$ (c). The shaded bands indicate statistical errors.

is needed to extract important information on the QCD phase diagram from experimental data.

Acknowledgments

BPS and CS are supported under DOE Contract No. DE-SC0012704. This research used resources of the National Energy Research Scientific Computing Center, which is supported by the Office of Science of the U.S. Department of Energy under Contract No. DE-AC02-05CH11231. BPS acknowledges a DOE Office of Science Early Career Award. CS thanks a Goldhaber Distinguished Fellowship from Brookhaven Science Associates. AM is supported by JSPS Overseas Research Fellowship. GSD thanks Conselho Nacional de Desenvolvimento Científico e Tecnológico (CNPq) for financial support. CG gratefully acknowledges support from the Canada Council for the Arts through its Killam Research Fellowship program. This work was supported in part by the Natural Sciences and Engineering Research Council of Canada. Computations were made in part on the supercomputer Guillimin from McGill University, managed by Calcul Québec and Compute Canada. The operation of this supercomputer is funded by the Canada Foundation for Innovation (CFI), NanoQuébec, RMGA and the Fonds de recherche du Québec - Nature et technologies (FRQ-NT). This work is supported in part by the U.S. Department of Energy, Office of Science, Office of Nuclear Physics, within the framework of the Beam Energy Scan Theory (BEST) Topical Collaboration.

Appendix A: Off-equilibrium corrections to the Cooper-Frye Freeze-out

In this appendix, we derive the out-of-equilibrium correction for the Cooper-Frye freeze-out procedure from particle diffusion effects. The system's energy-momentum tensor and conserved currents can be expressed as,

$$T^{\mu\nu} = \sum_{i=1}^{N} g_i \int dK_i k_i^\mu k_i^\nu f_i, \tag{A1}$$

$$N_Q^\mu = \sum_{i=1}^{N} g_i Q_i \int dK_i k_i^\mu f_i, \tag{A2}$$

where N_Q is the conserved charge in the system, g_i is the degeneracy factor, $Q_i = b_i, s_i, c_i$ is the charge, and $\int dK_i = \int \frac{d^3K_i}{(2\pi)^3 E_i}$. The Landau matching condition can be written as,

$$u_\mu u_\nu \delta T^{\mu\nu} = \sum_{i=1}^{N} g_i \int dK_i E_i^2 \delta f_i = 0, \tag{A3}$$

$$\Delta^{\mu\alpha} u^\beta \delta T_{\alpha\beta} = \sum_{i=1}^{N} g_i \int dK_i E_i k_i^{\langle\mu\rangle} \delta f_i = 0, \tag{A4}$$

$$u_\mu \delta N_Q^\mu = \sum_{i=1}^{N} g_i Q_i \int dK_i E_i \delta f_i = 0, \tag{A5}$$

where $k^{\langle\mu\rangle} = \Delta^{\mu\nu}k_\nu$. The dissipative quantities of the system can be computed as,

$$\Pi = -\frac{1}{3}\sum_{i=1}^{N} g_i m_i^2 \int dK_i \delta f_i, \tag{A6}$$

$$q_Q^\mu = \sum_{i=1}^{N} g_i Q_i \int dK_i k_i^{\langle\mu\rangle} \delta f_i, \tag{A7}$$

and

$$\pi^{\mu\nu} = \sum_{i=1}^{N} g_i \int dK_i k_i^{\langle\mu} k_i^{\nu\rangle} \delta f_i. \tag{A8}$$

The first-order Chapman-Enskog approximation [50] of the Boltzmann equation leads to

$$Df_i^{(0)} + \frac{1}{E_k^i} k_i^\mu \nabla_\mu f_i^{(0)} = \frac{1}{E_k^i} C[f_i^{(1)}], \tag{A9}$$

where $C[f_{ik}^{(1)}]$ is the linearized collision term. In the relaxation time approximation,

$$C[f_i^{(1)}] = -\frac{E_k^i}{\tau_R}\delta f_i, \tag{A10}$$

where τ_R is the relaxation time. The right hand side of Eq. (A9) becomes $-\frac{1}{\tau_R}\delta f_i$. On the left hand side, we have the equilibrium part of the distribution function,

$$f_i^{(0)} = \frac{1}{\exp[\beta_0(u_\mu k_i^\mu - Q_i\alpha_Q)] + \theta_i}, \tag{A11}$$

where $\beta_0 = 1/T$, $\alpha_Q = \mu_Q/T$, and $\theta_i = 1$ for fermions and $\theta_i = -1$ for bosons. Then

$$\begin{aligned}\delta f_i^{(0)} &= -f_i^{(0)}\tilde{f}_i^{(0)}[\delta\beta_0 u_\mu k_i^\mu + \beta_0 \delta u_\mu k_i^\mu \\ &\quad - Q_i \delta\alpha_Q]\end{aligned} \tag{A12}$$

with

$$\tilde{f}_i^{(0)} = (1 - \theta_i f_i^{(0)}). \tag{A13}$$

Next, insert them into Eq. (A9) and organize the terms into bulk, particle diffusion, and shear corrections according to the rank of the tensor (and the requirement of tracelessness for the shear correction). For particle diffusion, collecting all rank 1 terms leads to

$$\begin{aligned}\delta f_i^{\rm diffusion} &= f_i^{(0)}\tilde{f}_i^{(0)}\tau_R\Big[\beta_0 k_i^\mu Du_\mu + k_i^\mu(\nabla_\mu\beta_0) \\ &\quad - \frac{Q_i}{E_i}k_i^\mu\nabla_\mu\alpha_Q\Big].\end{aligned} \tag{A14}$$

Now, we need to replace all the time derivatives in δf using thermodynamic relations and first order conservation laws. The thermodynamic relations that we will use are,

$$dP_0 = s_0 dT + n_Q d\mu_Q \tag{A15}$$

$$\varepsilon_0 + P_0 = Ts_0 + \mu_Q n_Q. \tag{A16}$$

$$d\varepsilon_0 = Tds_0 + \mu_Q dn_Q \tag{A17}$$

Using the chain rule,

$$dT = -\frac{1}{\beta_0^2}d\beta_0 \tag{A18}$$

$$\beta_0 d\mu_Q = d\alpha_Q - \alpha_Q\frac{d\beta_0}{\beta_0} \tag{A19}$$

The conservation laws at first order in Knudsen number are,

$$D\varepsilon_0 = -(\varepsilon_0 + P_0)\theta \tag{A20}$$

$$(\varepsilon_0 + P_0)Du^\mu = \nabla^\mu P_0 \tag{A21}$$

$$Dn_Q = -n_Q\theta \tag{A22}$$

For diffusion in Eq. (A14),

$$\begin{aligned}\delta f_i^{\rm diffusion} &= f_i^{(0)}\tilde{f}_i^{(0)}\tau_R\Big[\frac{n_Q}{\varepsilon_0 + P_0}k_i^\mu\nabla_\mu\alpha_Q \\ &\quad - \frac{Q_i}{E_{ik}}k_i^\mu\nabla_\mu\alpha_Q\Big]\end{aligned} \tag{A23}$$

All the δfs are proportional to the relaxation time τ_R. In the following we derive expressions for the relaxation time in terms of the system's heat conductivity. In the Navier-Stokes limit, we have,

$$q_Q^\mu = \kappa\nabla^\mu\alpha_Q. \tag{A24}$$

Here we define useful thermodynamic integrals

$$J_{nq}^i = \frac{1}{(2q+1)!!}\int dK_i (u_\mu k_i^\mu)^{n-2q}(-\Delta_{\mu\nu}k_i^\mu k_i^\nu)^q f_{ik}^{(0)}\tilde{f}_{ik}^{(0)}. \tag{A25}$$

For charge diffusion, the situation for net baryon, net strangness, and net charge are very similar. So here we only consider net baryon charge as an example. Inserting Eq. (A23) into Eq. (A7) we find,

$$\begin{aligned}q_B^\mu &= \sum_{i=1}^{N} g_i b_i \int dK_i k_i^{\langle\mu\rangle}\delta f_k^i \\ &= \tau_R\Delta^\mu{}_\nu\nabla_\alpha\alpha_B\sum_{i=1}^{N} g_i b_i \\ &\quad\times\int dK_i k_i^\nu k_i^\alpha f_{ik}^{(0)}\tilde{f}_{ik}^{(0)}\tau_R\left[\frac{n_B}{\varepsilon_0+P_0} - \frac{b_i}{E_{ik}}\right]\end{aligned}$$

We define

$$I_B^{\nu\alpha} = \sum_{i=1}^{N} g_i b_i \int dK_i k_i^\nu k_i^\alpha f_{ik}^{(0)}\tilde{f}_{ik}^{(0)}\left[\frac{n_B}{\varepsilon_0+P_0} - \frac{b_i}{E_{ik}}\right]$$

and

$$q_B^\mu = \kappa_B \nabla^\mu \alpha_B = \tau_R \hat{\kappa}_B \nabla^\mu \alpha_B,$$

where

$$\begin{aligned}\hat{\kappa}_B &= \frac{1}{3}\Delta_{\mu\nu} I_B^{\mu\nu} \\ &= -\sum_{i=1}^{N_B}\left[\frac{n_B}{\varepsilon_0 + P_0} b_i J_{21}^i - J_{11}^i\right].\end{aligned}$$

Here N_B runs over all the baryons. In the massless limit,

$$\kappa_B = \tau_R n_B \left(\frac{1}{3}\coth\left(\alpha_B\right) - \frac{n_B T}{\varepsilon_0 + P_0}\right). \tag{A26}$$

In the small α_B limit

$$\kappa_B = \tau_R n_B \frac{1}{3\alpha_B} = \frac{\tau_R T}{3}\frac{n_B}{\mu_B}. \tag{A27}$$

In the relaxation time approximation, we can relate the net baryon diffusion constant to the specific shear viscosity through the relaxation time,

$$\tau_R = \frac{5\eta}{e + P} \tag{A28}$$

then

$$\kappa_B = \frac{5\eta}{e+\mathcal{P}}\frac{T}{3}\frac{n_B}{\mu_B} = \frac{5}{3}\frac{\eta T}{e+\mathcal{P}}\frac{n_B}{\mu_B}. \tag{A29}$$

For a small specific shear viscosity $\frac{\eta T}{e+\mathcal{P}} = \frac{1}{4\pi}$,

$$\kappa_B = \frac{5}{12\pi}\frac{n_B}{\mu_B}. \tag{A30}$$

The net baryon diffusion out-of-equilibrium correction to the Cooper-Frye formula δf is

$$\delta f_{ik}^{B-\text{diffusion}} = f_{ik}^{(0)}\tilde{f}_{ik}^{(0)}\left[\frac{n_B}{\varepsilon_0 + P_0} - \frac{b_i}{E_{ik}}\right]\frac{k_i^\mu q_\mu}{\hat{\kappa}_B}. \tag{A31}$$

Appendix B: Particlization at finite baryon density

In this appendix, we discuss about how to generate Monte-Carlo samples of particles from a hydrodynamic hypersurface with finite baryon chemical potential and baryon diffusion current.

Different species of particles and unstable resnonances are sampled one by one. For a given particle species, we first need to compute its particle yield in every freeze-out fluid cell. The space-time positions of the emitted particles are sampled from different freeze-out fluid cells with particle yields as relative weights. Sec. B 1 discuss how to compute the particle yield at finite baryon chemical potential and net baryon diffusion current. Once the particle's spatial position is determined, its momentum information is sampled using the acceptance-rejection method. This sampling method requires us to estimate the maximum of the particle momentum distribution. This is derived in Sec. B 2 with the presence of the net baryon diffusion out-of-equilibrium correction for the first time. All the numerics were implemented in the open-source iSpectraSampler (iSS) code package. The numerical validation is presented in Sec. B 3.

1. Estimation of particle yields

Particle momentum distributions from a fluid cell can be calculated using the Cooper-Frye formula,

$$E\frac{dN_i}{d^3p} = \frac{g_i}{(2\pi)^3}\Delta^3\sigma_\mu p^\mu (f_i^{(0)} + \delta f_i). \tag{B1}$$

So the particle yield is given by

$$N_i = \frac{g_i}{(2\pi)^3}\Delta^3\sigma_\mu \int \frac{d^3p}{E} p^\mu (f_i^{(0)} + \delta f_i). \tag{B2}$$

For the thermal equilibrium part,

$$f_i^{(0)} = \frac{1}{e^{\beta(E-\mu_i)} - \theta} \tag{B3}$$

with $\theta = -1$ for fermions and $\theta = +1$ for bosons. The equilibrium part of the integral can be evaluated as follows,

$$\begin{aligned}N_i^{\text{eq}} &= \frac{g_i}{(2\pi)^3}\Delta^3\sigma_\mu \int \frac{d^3p}{E} p^\mu \frac{1}{e^{\beta(E-\mu_i)} - \theta} \\ &= \frac{g_i}{2\pi^2}\Delta^3\sigma_\mu u^\mu \int dE E\frac{\sqrt{E^2 - m_i^2}}{e^{\beta(E-\mu_i)} - \theta}.\end{aligned} \tag{B4}$$

Now, we can expand the thermal equilibrium distribution function,

$$\frac{1}{e^{\beta(E-\mu_i)} - \theta} = \sum_{n=1}^{\infty}\theta^{n-1} e^{n\beta\mu_i} e^{-n\beta E}. \tag{B5}$$

In practice, we compute the summation up to $n = 10$. Thus,

$$N_i^{\text{eq}} = \frac{g_i}{2\pi^2}\Delta^3\sigma_\mu u^\mu \frac{m_i^2}{\beta}\sum_{n=1}^{\infty}\frac{\theta^{n-1}}{n} e^{n\beta\mu_i} K_2(n m_i \beta). \tag{B6}$$

Now, we focus on the contribution from baryon diffusion in the following because shear viscous effects do not modify the particle number and bulk viscosity is not considered in this work. The form of the off-equilibrium correction to the distribution function from net baryon diffusion is computed in the relaxation time approximation and given by (A31). This leads to a correction to the particle yield of the form

$$\begin{aligned}\delta N_i^q &= \frac{g_i \Delta^3\sigma_\mu}{(2\pi)^3}\int \frac{d^3p}{E}\frac{p^\mu p^\nu q_\nu}{\hat{\kappa}(T,\mu_B)} f_i^{(0)}\tilde{f}_i^{(0)}\left(\frac{n_B}{\varepsilon + \mathcal{P}} - \frac{b_i}{E}\right) \\ &= \frac{g_i}{(2\pi)^3}\frac{\Delta^3\sigma_\mu q^\mu}{\hat{\kappa}(T,\mu_B)} I(T, m_i)\end{aligned} \tag{B7}$$

with

$$I(T,m_i) = \frac{\Delta_{\mu\nu}}{3}\int\frac{d^3p}{E}p^\mu p^\nu f_i^{(0)}\tilde{f}_i^{(0)}\left(\frac{n_B}{\varepsilon+\mathcal{P}}-\frac{b_i}{E}\right)$$
$$= 4\pi\Bigg[-\frac{n_B}{\varepsilon+\mathcal{P}}\left(\frac{m_i^2}{\beta^2}\sum_{n=1}^{\infty}\frac{\theta^{n-1}}{n}e^{n\beta\mu_i}K_2(nm_i\beta)\right)$$
$$-b_i\left(\frac{1}{3\beta^3}\sum_{n=1}^{\infty}n\theta^{n-1}e^{n\beta\mu_i}I_1(m_i\beta,n)\right)\Bigg]$$

The second integral

$$I_1(m_i\beta,n)\equiv\int_{m_i\beta}^{\infty}\frac{d\xi}{\xi}\left(-\sqrt{\xi^2-(m_i\beta)^2}\right)^3e^{-n\xi} \quad \text{(B8)}$$

does not have a closed form, but can be expanded as follows

$$I_1(m_i\beta,n) = -(m_i\beta)^3\Bigg[\frac{e^{-nm_i\beta}}{nm_i\beta}\left(\frac{2}{(nm_i\beta)^2}+\frac{2}{nm_i\beta}-\frac{1}{2}\right)$$
$$+\sum_{k=3}^{\infty}\frac{3}{k!}\frac{(2k-5)!!}{2^k}E_{2k-2}(nm_i\beta)$$
$$+\frac{3}{8}E_2(nm_i\beta)\Bigg], \quad \text{(B9)}$$

where $E_k(nm_i\beta)$ is the exponential integral function. Finally, the correction to the particle yield from the baryon diffusion term becomes

$$\delta N_i^q = \frac{g_i}{2\pi^2}\frac{\Delta^3\sigma_\mu q^\mu}{\hat{\kappa}(T,\mu_B)}$$
$$\times\Bigg\{-\frac{n_B}{\varepsilon+\mathcal{P}}\left(\frac{m_i^2}{\beta^2}\left[\sum_{n=1}^{\infty}\frac{\theta^{n-1}}{n}e^{n\beta\mu_i}K_2(nm_i\beta)\right]\right)$$
$$-b_i\left(\frac{1}{3\beta^3}\left[\sum_{n=1}^{\infty}n\theta^{n-1}e^{n\beta\mu_i}I_1(m_i\beta,n)\right]\right)\Bigg\} \quad \text{(B10)}$$

In the numerical implementation, we truncate the summations in Eqs. (B9) and (B10) at $n=10$.

2. Estimation of the maximum in the particle distribution

In the processes of sampling, we need to estimated the maximum of the particle momentum distribution, $E\frac{dN}{d^3p}$. Using the Hölder inequality [51], we have

$$p^\mu\Delta^3\sigma_\mu < (p\cdot u)\left(|\Delta^3\sigma_\mu u^\mu|+\sqrt{|\Delta^3\sigma_\mu\Delta^3\sigma_\nu\Delta^{\mu\nu}|}\right). \quad \text{(B11)}$$

In order to estimate the maximum of the particle distribution, it is useful to define the following function [51],

$$G(E;A,\theta)=\frac{E^A}{e^{\beta(E-\mu)}-\theta}. \quad \text{(B12)}$$

By setting its derivatives to zero, the extrema can be computed and denoted as $G_{\max}^{(A,\theta)}$. The detailed expression of $G_{\max}^{(A,\theta)}$ was discussed in Ref. [51]. For the equilibrium part we need to calculate the maximum of the function

$$Ef_0=\frac{E}{e^{\beta(E-\mu_i)}-\theta}=G(E;1,\theta) \quad \text{(B13)}$$

The solution is $G_{\max}^{(1,\theta)}$.

For baryon diffusion we have

$$E\delta f_q < \frac{\sqrt{-q^\mu q_\mu}}{\hat{\kappa}(T,\mu_B)}\left(\frac{n_B}{\varepsilon+\mathcal{P}}\lambda G_{\max}^{(2,\theta)}+|b_i|\lambda G_{\max}^{(1,\theta)}\right) \quad \text{(B14)}$$

and the shear viscous correction yields

$$E\delta f_\pi < \frac{\sqrt{\pi^{\mu\nu}\pi_{\mu\nu}}}{2(\varepsilon+\mathcal{P})T}\lambda G_{\max}^{(2,\theta)}. \quad \text{(B15)}$$

Here $\lambda=1$ for fermions and $\lambda=2$ for bosons.

So the maximum of the particle momentum spectra can be estimated as,

$$P_{\max} = \frac{g_a}{(2\pi)^3}\left(|\Delta^3\sigma_\mu u^\mu|+\sqrt{|\Delta^3\sigma_\mu\Delta^3\sigma_\nu\Delta^{\mu\nu}|}\right)$$
$$\times\Bigg(G_{\max}^{(1,\theta)}$$
$$+\frac{\sqrt{-q^\mu q_\mu}}{\hat{\kappa}(T,\mu_B)}\left(\frac{n_B}{\varepsilon+\mathcal{P}}\lambda G_{\max}^{(2,\theta)}+|b_i|\lambda G_{\max}^{(1,\theta)}\right)$$
$$+\frac{\sqrt{\pi^{\mu\nu}\pi_{\mu\nu}}}{2(\varepsilon+\mathcal{P})T}\lambda G_{\max}^{(2,\theta)}\Bigg) \quad \text{(B16)}$$

3. Validation of the particle sampling procedure

In this section we present a validation of the numerical particle sampler by comparing to results computed directly from the Cooper-Frye formula. Individual particles are sampled from a (3+1)D hydrodynamic hyper-surface for 10-40% Au+Au collisions at 19.6 A GeV. We include effects from finite net baryon density and net baryon diffusion to the particle momentum distribution. The net baryon diffusion coefficient is set to $\kappa=0.2n_B/\mu_B$ in the hydrodynamic simulation.

Please note that the Cooper-Frye results shown in this section are produced using MUSIC, which is completely independent of the particle sampler iSS. Hence, the following numerical comparisons also provide a cross check of computing particle momentum distributions using the Cooper-Frye procedure in the two numerical codes.

As presented in Figs. 15, 16, and 17, the particle sampler iSS reproduces the numerical results from the Cooper-Frye formula as desired. Particle pseudo-rapidity distributions, p_T-spectra, and p_T-differential elliptic flow coefficients $v_2(p_T)$ are shown to be in good agreement between the two numerical codes. Out-of-equilibrium corrections from shear viscosity and net baryon diffusion are included in the calculations.

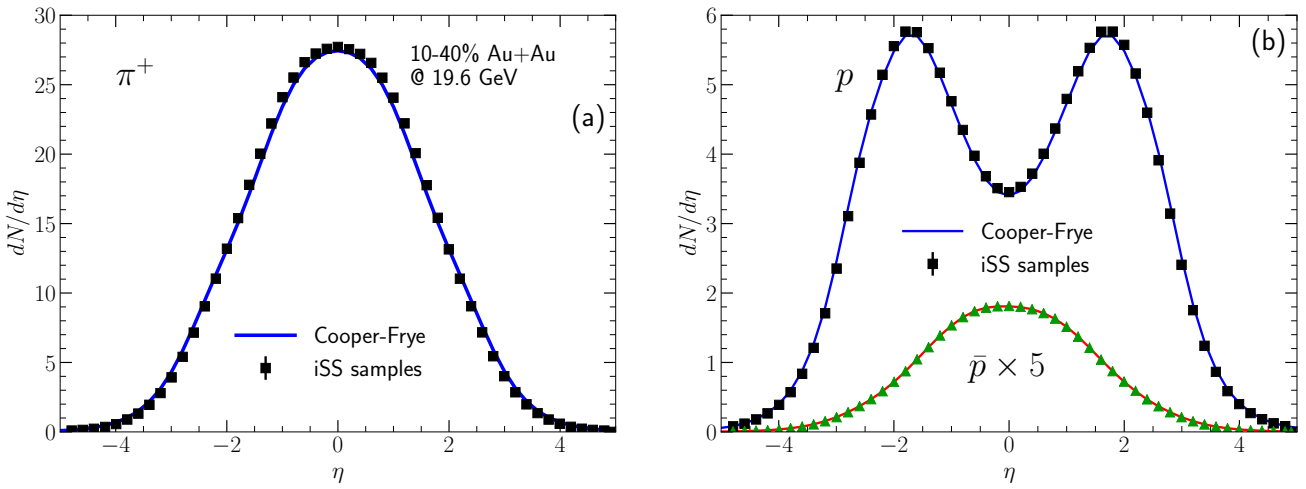

FIG. 15: Cross check the pseudo-rapidity distribution of thermally emitted π^+, p, and $\bar{p}$ between the numerical results from Cooper-Frye formula (lines) and the statistical results from particle sampler `iSS` (markers).

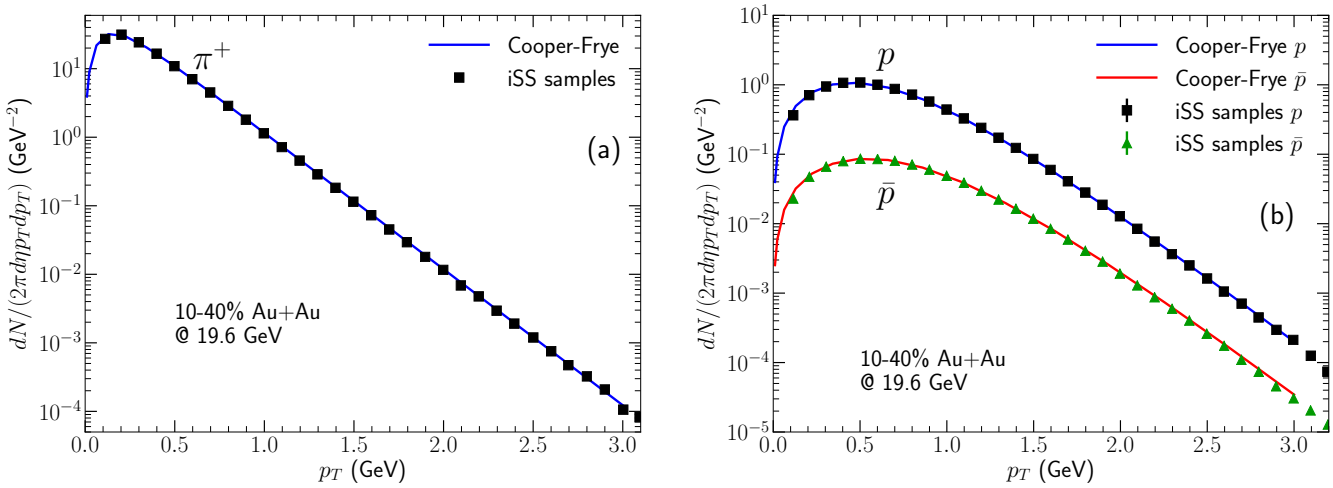

FIG. 16: Cross check the p_T-spectra of thermally emitted π^+, p, and $\bar{p}$ between the numerical results from Cooper-Frye formula (lines) and the statistical results from particle sampler `iSS` (markers).

Appendix C: Validation of hydrodynamic evolution at finite baryon density

In this appendix, we provide two numerical checks for the hydrodynamic evolution at finite baryon density.

1. Gubser Solution at finite μ_B

Similar to the analyses performed in Ref. [52], we use hydrodynamic solutions obtained assuming a Gubser flow background [53, 54] to test our simulation code. These types of solutions display a strong radial expansion rate and allow us to check the performance of our code in the transverse plane. We note that the Gubser solutions are valid only for conformal fluids and, in this sense, they assume an ideal equation of state, $\varepsilon \sim T^4$, $P \sim T^4$, and $\varepsilon = 3P$. Furthermore, such solutions cannot display any effects of diffusion, since the only scale present in the problem is the temperature and, consequently, the chemical potential must behave as $\mu_B \sim T$. This leads to a thermal potential μ_B/T that is constant and to a vanishing Navier-Stokes term $\nabla^\mu (\mu_B/T) = 0$. Nevertheless, we can still test the code in the ideal fluid limit, in the presence of a finite net-charge (here, the baryon number) density (this will keep $\varepsilon \sim P \sim T^4$, and $\varepsilon = 3P$, only changing the proportionality factors between ε, P and T^4).

In the ideal fluid limit, an analytic solution of the velocity, energy density and net-charge density were obtained in Refs. [53, 54]. Such solutions provides us with a non-

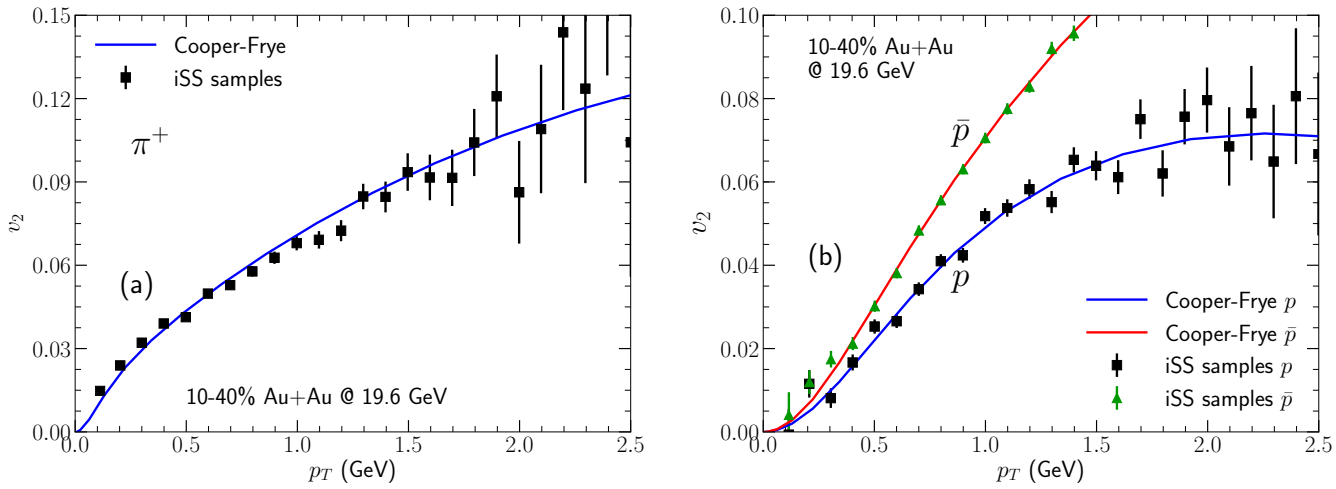

FIG. 17: Cross check the p_T-differential v_2 of thermally emitted π^+, p, and $\bar{p}$ between the numerical results from Cooper-Frye formula (lines) and the statistical results from particle sampler `iSS` (markers).

trivial numerical check for the dynamical evolution of ρ_B in the transverse plane. The analytic solutions for the hydrodynamic fields are,

$$e(\tau, r) = \frac{e_0}{\tau^4} \frac{(2q\tau)^{8/3}}{[1 + 2q^2(\tau^2 + r^2) + q^4(\tau^2 - r^2)^2]^{4/3}} \quad \text{(C1)}$$

$$n_B(\tau, r) = \frac{n_{B0}}{\tau^3} \frac{4q^2\tau^2}{[1 + 2q^2(\tau^2 + r^2) + q^4(\tau^2 - r^2)]^2} \quad \text{(C2)}$$

with the radial velocity being given by (this radial velocity is unaffected by the inclusion of viscosity or of a finite baryon density)

$$v^r(\tau, r) = \frac{2q^2\tau r}{1 + (q\tau)^2 + (qr)^2}, \quad \text{(C3)}$$

where $r = \sqrt{x^2 + y^2}$ is the transverse radius. The constant q, introduced in the expressions above, is a free parameter of the solution and determines the system size, with larger values of q corresponding to smaller systems. In our simulations, we fix $q = 1$ fm^{-1} – the same value as used in Ref. [52]. Also, $e_0 = 1$ fm^{-4} and $\rho_{B0} = 0.5$ fm^{-3} are free parameters that determine the initial value at, $r = 0$, of the energy and net-charge densities.

Figure 18 shows the comparison between numerical solutions found using MUSIC (dark dashed lines) and the analytic solution (light solid lines). An excellent agreement is obtained over the entire space ($r < 5$ fm) for all times between 1 fm$< \tau <$ 3.0 fm. We note that, even though we only considered a time evolution of 2 fm, this was enough for the charge density of the fluid to decrease by a factor ∼100 and that MUSIC was able to describe the solution over such a wide range of densities.

2. Cross check hydrodynamic evolution with net baryon diffusion in 1+1D

We next present a comparison of the evolution including net baryon diffusion with numerical solutions in longitudinal 1+1D [55]. The equations of motion are as follows,

$$\partial_\mu T^{\mu\nu} = 0; \quad \partial_\mu J^\mu_B = 0 \quad \text{(C4)}$$

with $J^\mu_B = n_B u^\mu + q^\mu$. The baryon diffusion current q^μ evolves with

$$\Delta^{\mu\nu} D q_\nu = -\frac{1}{\tau_q}\left(q^\mu - \kappa \nabla^\mu \frac{\mu_B}{T}\right). \quad \text{(C5)}$$

In the numerical test shown in Fig. 19, the net baryon diffusion coefficient is chosen to be $\kappa = 0.2 n_B/\mu_B$ and the diffusion relaxation time, $\tau_q = 0.2/T$. Good agreements are achieved for the rapidity evolution of local energy density and net baryon density between the two numerical algorithms. This validates our numerical solver with baryon diffusion along the longitudinal direction.

3. Stabilized numerical evolution with net baryon diffusion

Viscous hydrodynamics considers the net baryon diffusion current q^μ as a perturbative correction to the equilibrium net baryon current. However, the size of q^μ can be comparable or even larger than n_B in dilute density regions in realistic event-by-event simulations. Although these fluid cells are far outside the freeze-out surface and their dynamical evolution does not affect any physical observables, they may cause numerical instability problems during the evolution. To stabilize the simulations, we regulate the ill-behaved q^μ in fluid cells.

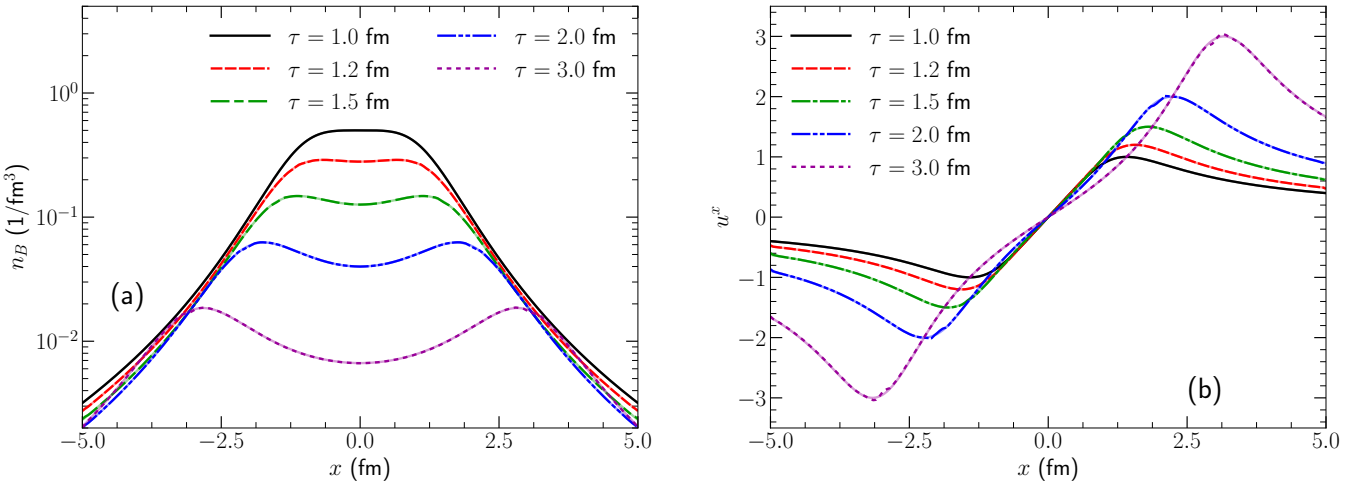

FIG. 18: The evolution of n_B and flow velocity u^x compared with analytic Gubser solution (light solid lines in the background).

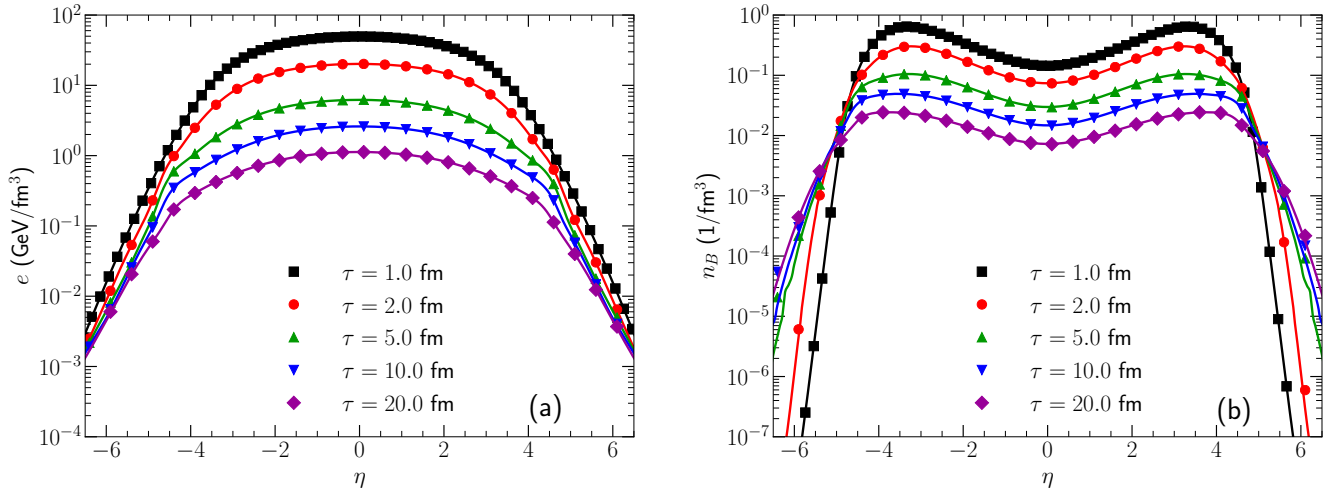

FIG. 19: The evolution of local energy density e and net baryon density n_B compared with (1+1)-D numerical solutions (markers).

First we need to make sure that the diffusion current is orthogonal to the flow velocity u^μ. This is done by evolving the three spatial components of q^μ as independent fields, while the q^τ component is constructed using $q^\tau = q^i u_i/u^\tau$ where i is summed over x, y, and η. Secondly, the relative size of q^μ compared to the net baryon density n_B can be computed as,

$$r_q = \frac{1}{f_{\rm strength}}\sqrt{\frac{q^\mu q_\mu}{n_B^2}}, \tag{C6}$$

where the regulation strength parameter

$$f_{\rm strength} = \chi_0\left[\frac{1}{\exp(-(e-e_0)/\xi_0)+1} - \frac{1}{\exp(e_0/\xi_0)+1}\right]. \tag{C7}$$

The parameter χ_0 controls the overall strength of the regulation for local energy density e above a critical energy density e_0. For the fluid cell whose local energy density is smaller than e_0, the regulation strength increases exponentially as the local energy density e decreases. In Eq. (C7), we chose $\chi_0 = 10$, $e_0 = 0.1\,\mathrm{GeV/fm^3}$, and the width parameter $\xi_0 = 0.01\,\mathrm{GeV/fm^3}$.

When the ratio r_q is larger than some maximum value $r_q^{\rm max}$, the q^μ current is regulated as,

$$\tilde{q}^\mu = \frac{r_q^{\rm max}}{r_q} q^\mu. \tag{C8}$$

With this regulation scheme, we found that 100% of event-by-event hydrodynamic simulations could be stabilized with $r_q^{\rm max} = 1$.

We have checked that the majority of the regulations are triggered in the dilute density region outside the freeze-out surface, leaving the physical region untouched.

The final hadronic flow observables show negligible dependence on ξ_0 in the range of 1 to 30.

Appendix D: Comparison between two microscopic hadronic transport models: UrQMD and JAM

In this section, we use the same inputs for two publicly available hadronic transport codes and compare the final hadronic observables. The difference from the two hadronic cascade models can help us to estimate theoretical uncertainties in the late dilute phase.

Figures 20, 21, and 22 show the comparisons between the two hadronic transport models. We find identical results for charged hadron pseudorapidity distributions and p_T-spectra of π^+ and K^+. This means that the dynamical evolution of the light mesons are very close in the two hadronic cascade models. Meanwhile, small but visible differences are present in proton and antiproton transverse momentum and rapidity distributions. The net proton numbers from the JAM model are slightly smaller than those from UrQMD. This might indicate a slightly stronger baryon-anti-baryon annihilation in the JAM model. The p_T spectrum of protons from the JAM model is slightly steeper than that from UrQMD. The two transport models also produce slightly different results for π^+ and p p_T differential elliptic flow. The JAM model gives smaller v_2 value compared to the UrQMD results, which is statistically significant for $p_T < 1\,\mathrm{GeV}$.

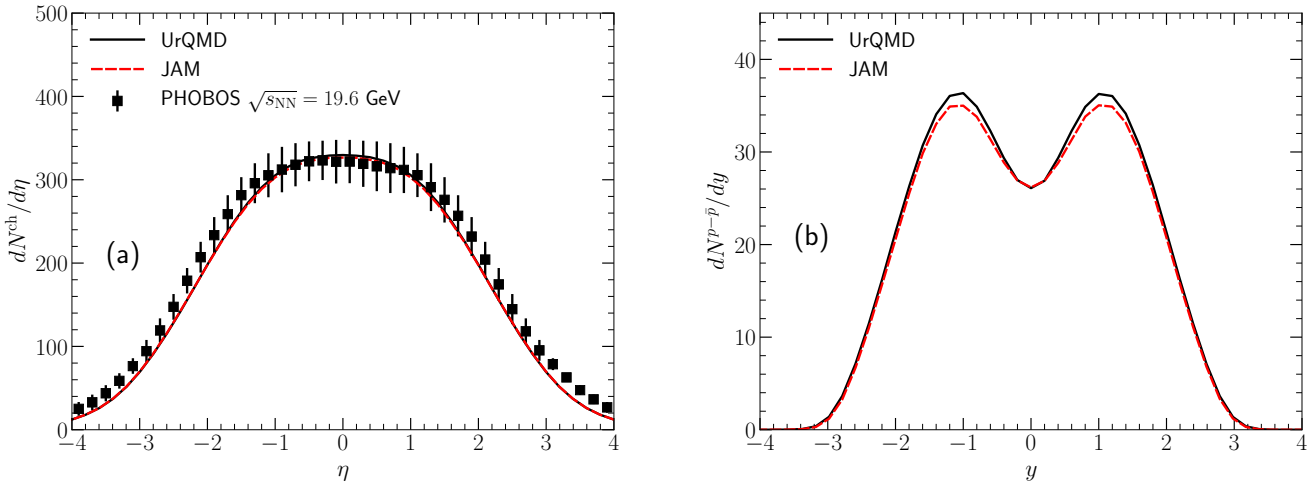

FIG. 20: The (pseudo-)rapidity distribution of charged hadrons (a) and net protons (b) from the two hadronic cascade simulations for 0-5% centrality Au+Au collisions at 19.6 GeV.

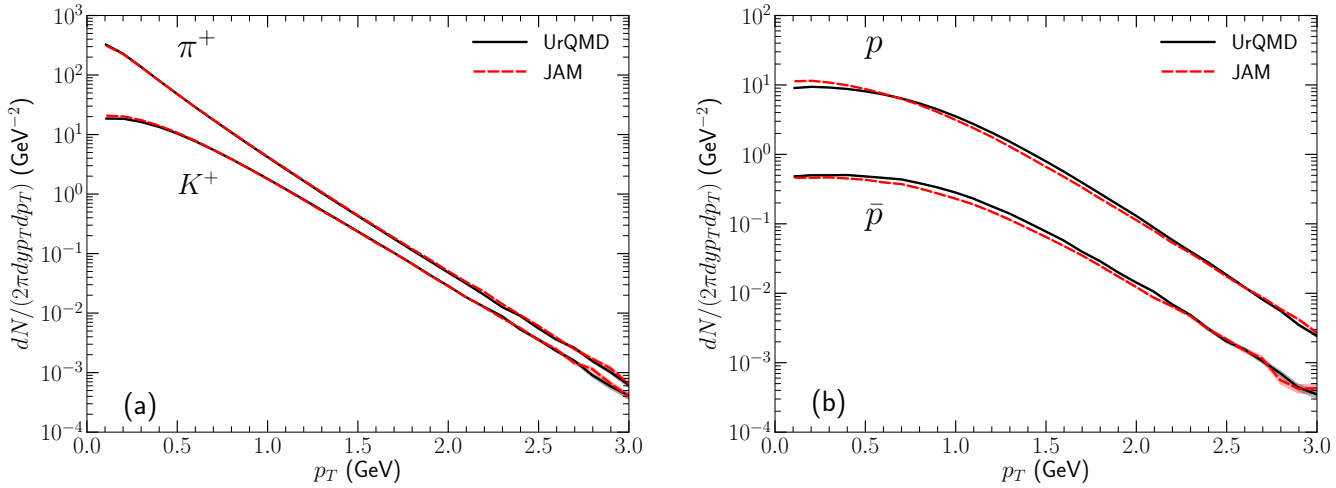

FIG. 21: The comparison of p_T-spectra of final π^+ and K^+ (panel (a)) and p and $\bar{p}$ (panel (b)) from the two hadronic cascade simulations.

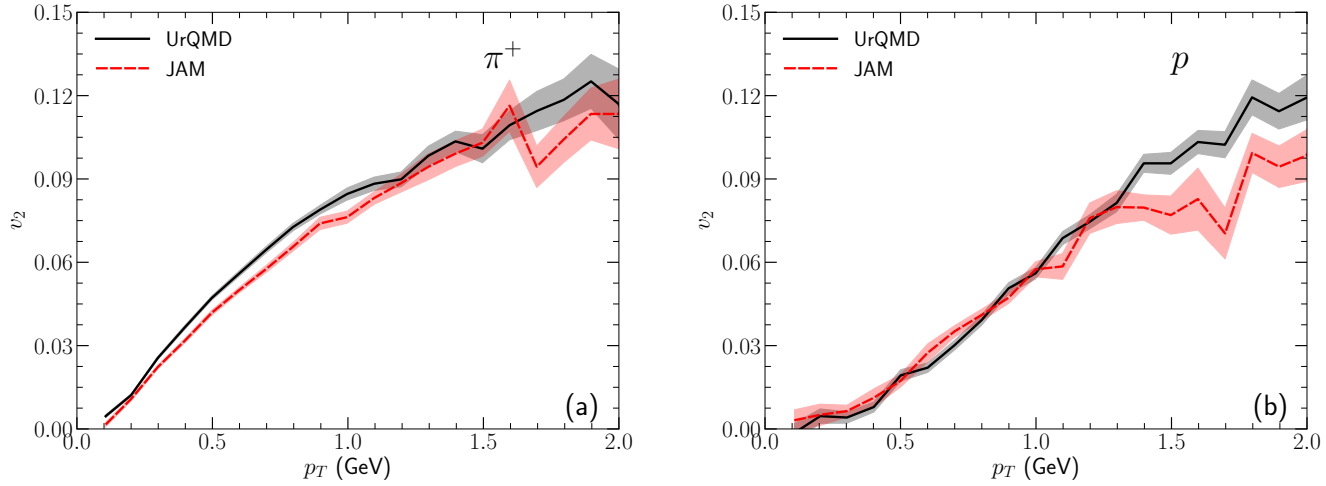

FIG. 22: The p_T-differential v_2 of final π^+ and K^+ (panel (a)) and p (panel (b)) from the two hadronic cascade simulations. The shaded bands indicate statistical errors.

[1] L. Adamczyk et al. (STAR), Phys. Rev. Lett. **112**, 032302 (2014), 1309.5681.
[2] L. Adamczyk et al. (STAR), Phys. Rev. Lett. **113**, 092301 (2014), 1402.1558.
[3] A. Adare et al. (PHENIX), Phys. Rev. **C93**, 011901 (2016), 1506.07834.
[4] L. Adamczyk et al. (STAR), Phys. Rev. **C96**, 044904 (2017), 1701.07065.
[5] M. Mackowiak-Pawlowska (NA61/SHINE), in *9th Workshop "Excited QCD" 2017 Sintra, Portugal, May 7-13, 2017* (2017), 1707.04735, URL http://inspirehep.net/record/1610347/files/arXiv:1707.04735.pdf.
[6] M. A. Stephanov, K. Rajagopal, and E. V. Shuryak, Phys. Rev. Lett. **81**, 4816 (1998), hep-ph/9806219.
[7] M. A. Stephanov, K. Rajagopal, and E. V. Shuryak, Phys. Rev. **D60**, 114028 (1999), hep-ph/9903292.
[8] M. A. Stephanov, Prog. Theor. Phys. Suppl. **153**, 139 (2004), [Int. J. Mod. Phys.A20,4387(2005)], hep-ph/0402115.
[9] J. I. Kapusta, B. Muller, and M. Stephanov, Phys. Rev. **C85**, 054906 (2012), 1112.6405.
[10] C. Young, J. I. Kapusta, C. Gale, S. Jeon, and B. Schenke, Phys. Rev. **C91**, 044901 (2015), 1407.1077.
[11] J. I. Kapusta and C. Young, Phys. Rev. **C90**, 044902 (2014), 1404.4894.
[12] W. Cassing and E. L. Bratkovskaya, Nucl. Phys. **A831**, 215 (2009), 0907.5331.
[13] I. A. Karpenko, P. Huovinen, H. Petersen, and M. Bleicher, Phys. Rev. **C91**, 064901 (2015), 1502.01978.
[14] P. Batyuk, D. Blaschke, M. Bleicher, Yu. B. Ivanov, I. Karpenko, S. Merts, M. Nahrgang, H. Petersen, and O. Rogachevsky, Phys. Rev. **C94**, 044917 (2016), 1608.00965.
[15] P. Batyuk, D. Blaschke, M. Bleicher, Yu. B. Ivanov, I. Karpenko, L. Malinina, S. Merts, M. Nahrgang, H. Petersen, and O. Rogachevsky, in *6th International Conference on New Frontiers in Physics (ICNFP 2017) Kolymbari, Crete, Greece, August 17-26, 2017* (2017), 1711.07959, URL http://inspirehep.net/record/1637369/files/arXiv:1711.07959.pdf.
[16] C. Shen and B. Schenke, Phys. Rev. **C97**, 024907 (2018), 1710.00881.
[17] Y. Akamatsu, M. Asakawa, T. Hirano, M. Kitazawa, K. Morita, K. Murase, Y. Nara, C. Nonaka, and A. Ohnishi (2018), 1805.09024.
[18] C. Nonaka and M. Asakawa, Phys. Rev. **C71**, 044904 (2005), nucl-th/0410078.
[19] K. Paech and A. Dumitru, Phys. Lett. **B623**, 200 (2005), nucl-th/0504003.
[20] C. Herold, M. Nahrgang, I. Mishustin, and M. Bleicher, Phys. Rev. **C87**, 014907 (2013), 1301.1214.
[21] S. Mukherjee, R. Venugopalan, and Y. Yin, Phys. Rev. **C92**, 034912 (2015), 1506.00645.
[22] U. Heinz and R. Snellings, Ann. Rev. Nucl. Part. Sci. **63**, 123 (2013), 1301.2826.
[23] C. Gale, S. Jeon, and B. Schenke, Int.J.Mod.Phys. **A28**, 1340011 (2013), 1301.5893.
[24] H. Petersen, J. Phys. **G41**, 124005 (2014), 1404.1763.
[25] M. Okai, K. Kawaguchi, Y. Tachibana, and T. Hirano, Phys. Rev. **C95**, 054914 (2017), 1702.07541.
[26] B. Schenke, S. Jeon, and C. Gale, Phys. Rev. **C82**, 014903 (2010), 1004.1408.
[27] J. I. Kapusta and C. Plumberg, Phys. Rev. **C97**, 014906 (2018), 1710.03329.
[28] B. B. Back et al. (PHOBOS), Phys. Rev. **C74**, 021901 (2006), nucl-ex/0509034.
[29] T. Anticic et al. (NA49), Phys. Rev. **C83**, 014901 (2011), 1009.1747.
[30] G. S. Denicol, T. Koide, and D. H. Rischke, Phys. Rev. Lett. **105**, 162501 (2010), 1004.5013.
[31] G. S. Denicol, H. Niemi, E. Molnar, and D. H. Rischke, Phys. Rev. **D85**, 114047 (2012), [Erratum: Phys. Rev.D91,no.3,039902(2015)], 1202.4551.
[32] E. Molnar, H. Niemi, G. S. Denicol, and D. H. Rischke, Phys. Rev. **D89**, 074010 (2014), 1308.0785.
[33] G. S. Denicol, S. Jeon, and C. Gale, Phys. Rev. **C90**, 024912 (2014), 1403.0962.
[34] A. Czajka, S. Hauksson, C. Shen, S. Jeon, and C. Gale (2017), 1712.05905.
[35] J. Gunther, R. Bellwied, S. Borsanyi, Z. Fodor, S. D. Katz, A. Pasztor, and C. Ratti (2016), 1607.02493.
[36] S. Borsanyi, Z. Fodor, C. Hoelbling, S. D. Katz, S. Krieg, and K. K. Szabo, Phys. Lett. **B730**, 99 (2014), 1309.5258.
[37] S. Borsanyi, Z. Fodor, S. D. Katz, S. Krieg, C. Ratti, and K. Szabo, JHEP **01**, 138 (2012), 1112.4416.
[38] P. Huovinen and P. Petreczky, Nucl. Phys. **A837**, 26 (2010), 0912.2541.
[39] A. Monnai and B. Schenke, Phys. Lett. **B752**, 317 (2016), 1509.04103.
[40] J. Cleymans, H. Oeschler, K. Redlich, and S. Wheaton, Phys. Rev. **C73**, 034905 (2006), hep-ph/0511094.
[41] F. Cooper and G. Frye, Phys. Rev. **D10**, 186 (1974).
[42] S. Ryu, J. F. Paquet, C. Shen, G. S. Denicol, B. Schenke, S. Jeon, and C. Gale, Phys. Rev. Lett. **115**, 132301 (2015), 1502.01675.
[43] M. Albright and J. I. Kapusta, Phys. Rev. **C93**, 014903 (2016), 1508.02696.
[44] A. Jaiswal, B. Friman, and K. Redlich, Phys. Lett. **B751**, 548 (2015), 1507.02849.
[45] A. Monnai (2018), 1803.03318.
[46] S. A. Bass et al., Prog. Part. Nucl. Phys. **41**, 255 (1998), [Prog. Part. Nucl. Phys.41,225(1998)], nucl-th/9803035.
[47] M. Bleicher et al., J. Phys. **G25**, 1859 (1999), hep-ph/9909407.
[48] Y. Nara, N. Otuka, A. Ohnishi, K. Niita, and S. Chiba, Phys. Rev. **C61**, 024901 (2000), nucl-th/9904059.
[49] M. Greif, J. A. Fotakis, G. S. Denicol, and C. Greiner (2017), 1711.08680.
[50] S. Chapman and T. Cowling, *The Mathematical Theory of Non-Uniform Gases* (Cambridge University Press, 1952).
[51] C. Shen, Z. Qiu, H. Song, J. Bernhard, S. Bass, and U. Heinz, Comput. Phys. Commun. **199**, 61 (2016), 1409.8164.
[52] H. Marrochio, J. Noronha, G. S. Denicol, M. Luzum, S. Jeon, and C. Gale, Phys. Rev. **C91**, 014903 (2015), 1307.6130.
[53] S. S. Gubser, Phys. Rev. **D82**, 085027 (2010), 1006.0006.
[54] S. S. Gubser and A. Yarom, Nucl. Phys. **B846**, 469 (2011), 1012.1314.
[55] A. Monnai, Phys. Rev. **C86**, 014908 (2012), 1204.4713.